

AFRL-PR-WP-TR-2003-2022

**THE APPLICATION OF ADVANCED
DIAGNOSTICS TO THE STUDY OF
NON-EQUILIBRIUM AIR PLASMAS**



**James M. Williamson, Ph.D.
Peter Bletzinger, Ph.D.**

**Innovative Scientific Solutions, Inc.
2766 Indian Ripple Road
Dayton, OH 45440-3638**

SEPTEMBER 2002

Final Report for 23 March 1998 – 01 June 2002

Approved for public release; distribution is unlimited.


**PROPULSION DIRECTORATE
AIR FORCE RESEARCH LABORATORY
AIR FORCE MATERIEL COMMAND
WRIGHT-PATTERSON AIR FORCE BASE, OH 45433-7251**


NOTICE


When Government drawings, specifications, or other data are used for any purpose other than in connection with a definitely Government-related procurement, the United States Government incurs no responsibility or any obligation whatsoever. The fact that the Government may have formulated or in any way supplied the said drawings, specifications, or other data, is not to be regarded by implication, or otherwise in any manner construed, as licensing the holder, or any other person or corporation; or as conveying any rights or permission to manufacture, use, or sell any patented invention that may in any way be related thereto.

This report is releasable to the National Technical Information Service (NTIS). At NTIS, it will be available to the general public, including foreign nations.

This technical report has been reviewed and is approved for publication.


BISWA N. GANGULY
Research Physicist, Plasma Physics Branch
Power Division
Propulsion Directorate


JOSEPH A. WEIMER
Chief, Plasma Physics Branch
Power Division
Propulsion Directorate


C. SCOTT RUBERTUS
Acting Deputy Chief
Power Division
Propulsion Directorate

If your address has changed, if you wish to be removed from our mailing list, or if the addressee is no longer employed by your organization, please notify AFRL/PRPE, 1950 Fifth Street, WPAFB, OH 45433-7251 to help us maintain a current mailing list.

Copies of this report should not be returned unless return is required by security considerations, contractual obligations, or notice on a specific document.

REPORT DOCUMENTATION PAGE				Form Approved OMB No. 0704-0188	
<p>The public reporting burden for this collection of information is estimated to average 1 hour per response, including the time for reviewing instructions, searching existing data sources, gathering and maintaining the data needed, and completing and reviewing the collection of information. Send comments regarding this burden estimate or any other aspect of this collection of information, including suggestions for reducing this burden, to Department of Defense, Washington Headquarters Services, Directorate for Information Operations and Reports (0704-0188), 1215 Jefferson Davis Highway, Suite 1204, Arlington, VA 22202-4302. Respondents should be aware that notwithstanding any other provision of law, no person shall be subject to any penalty for failing to comply with a collection of information if it does not display a currently valid OMB control number. PLEASE DO NOT RETURN YOUR FORM TO THE ABOVE ADDRESS.</p>					
1. REPORT DATE (DD-MM-YY) September 2002		2. REPORT TYPE Final		3. DATES COVERED (From - To) 03/23/1998 – 06/01/2002	
4. TITLE AND SUBTITLE THE APPLICATION OF ADVANCED DIAGNOSTICS TO THE STUDY OF NON-EQUILIBRIUM AIR PLASMAS				5a. CONTRACT NUMBER F33615-98-C-2806	
				5b. GRANT NUMBER	
				5c. PROGRAM ELEMENT NUMBER 61102F	
6. AUTHOR(S) James M. Williamson, Ph.D. Peter Bletzinger, Ph.D.				5d. PROJECT NUMBER 2301	
				5e. TASK NUMBER DW	
				5f. WORK UNIT NUMBER 11	
7. PERFORMING ORGANIZATION NAME(S) AND ADDRESS(ES) Innovative Scientific Solutions, Inc. 2766 Indian Ripple Road Dayton, OH 45440-3638				8. PERFORMING ORGANIZATION REPORT NUMBER	
9. SPONSORING/MONITORING AGENCY NAME(S) AND ADDRESS(ES) Propulsion Directorate Air Force Research Laboratory Air Force Materiel Command Wright-Patterson Air Force Base, OH 45433-7251				10. SPONSORING/MONITORING AGENCY ACRONYM(S) AFRL/PRPE	
				11. SPONSORING/MONITORING AGENCY REPORT NUMBER(S) AFRL-PR-WP-TR-2003-2022	
12. DISTRIBUTION/AVAILABILITY STATEMENT Approved for public release; distribution is unlimited.					
13. SUPPLEMENTARY NOTES This report contains color.					
14. ABSTRACT (Maximum 200 Words) Low-Mach-number shock waves propagating through a low-pressure, non-equilibrium, positive-column gas discharge have been observed to experience dispersion and velocity changes. These effects are shown to depend on discharge polarity. Optical and electrical measurements are described which demonstrate further polarity-dependent effects in discharge light emission and changes in electrical properties. The axial-population-density profile of 2^3S_1 metastable He has also been measured by diode-laser absorption spectroscopy in the double layer formed at an abrupt transition of the tube diameter in a positive column. The diode-laser absorption profiles show enhanced production of triplet metastable He 2^3S_1 in the double-layer region, as compared to that of the unperturbed positive column (small diameter), with the magnitude of being strongly dependent on the discharge polarity. The absolute concentration of H-atoms has been measured in the positive column of a pulsed dc discharge by two-photon-absorption laser-induced fluorescence (TALIF) in $H_2 - N_2$ gas mixtures at constant pressure and current for discharge-pulse durations of 10 μs to 1 ms. The change in H-atom production from the direct-electron-impact dissociation of H_2 at short times compared to that from multi-quantum vibrational energy-transfer-induced dissociation of H_2 at long times is determined from temporally resolved H-atom-concentration measurements.					
15. SUBJECT TERMS positive column, gas discharge, shock-wave propagation, metastable He, double layer, diode-laser absorption, H_2 dissociation, laser-induced fluorescence					
16. SECURITY CLASSIFICATION OF:			17. LIMITATION OF ABSTRACT: SAR	18. NUMBER OF PAGES 64	19a. NAME OF RESPONSIBLE PERSON (Monitor) Dr. Biswa N. Ganguly 19b. TELEPHONE NUMBER (Include Area Code) (937) 255-2923
a. REPORT Unclassified	b. ABSTRACT Unclassified	c. THIS PAGE Unclassified			

TABLE OF CONTENTS

<u>Section</u>	<u>Page</u>
SUMMARY	1
Shock Propagation in Plasmas	1
He-Metastable Density in a Double Layer	1
H-Atom Measurement in a H ₂ -N ₂ Pulsed Glow Discharge	2
INTRODUCTION	2
WORK ACCOMPLISHED	4
Shock Propagation in Plasmas	4
He-Metastable Density in a Double Layer	25
H-Atom Measurement in a H ₂ -N ₂ Pulsed Glow Discharge	33
REFERENCES	48
PRESENTATIONS	50
PUBLICATIONS	51

LIST OF FIGURES

<u>Figure</u>	<u>Page</u>
1 Experimental Setup for Measuring the Local Velocity at Two Positions in the Positive Column of a Gas Discharge	5
2 Laser Signals at Positions 40 and 169 mm from the Cathode in 15-Torr N ₂ . Note not only that the velocities are increasing in the discharge but also that the velocity at the downstream position, while lower in neutral gas, becomes higher than the upstream velocity when the discharge is on	6
3 Top - 337.1-nm Spatially Resolved Light Emission at a Location 36 mm from the Upstream Electrode and Laser-Photodeflection Signals; Middle - Discharge Voltages; Bottom - Discharge Currents for Case C (Solid Lines) and Case A (Dashed Lines). The two vertical lines indicate the time of arrival of the shock wave at the discharge and at the 36-mm measuring location, respectively	8
4 337.1-nm, Spatially Resolved Light Emission Measured at Four Positions from the Electrode Nearest the Spark Source. Also shown are the laser-photo-deflection signals at the same position	9
5 Discharge Voltages of the Second Discharge at a Second-Discharge Current of 100 mA, a Pressure 40-Torr N ₂ at Two Spark-Gap Capacitor Voltages, and Various Currents of the First Discharge	11
6 Change of the Second-Discharge Voltage (in Percent) as a Function of the First-Discharge Current and the Spark-Gap Capacitor Voltage	12
7 Discharge Voltage and Current and 337.1-nm Sidelight Emission for a 5-Torr, 50-mA Discharge in N ₂ ; 5 kV at 2-μF Spark Discharge	13
8 Discharge Voltage (Top), Floating-Probe Voltages and Their Difference (Bottom) for a Cathode-to-Anode Directed Shock Wave in 5-Torr N ₂ at 60-mA Discharge Current	14
9 Comparison of a) Difference in Floating-Probe Voltages, b) Differential-Probe Output, and c) 337.1-nm Collimated Sidelight Emission	16
10 Differential Probe Output at Three Locations along the Discharge	17
11 Images for a Cathode-to-Anode Propagating Shock	18
12 Images for an Anode-to-Cathode Propagating Shock	18
13 Images for a Cathode-to-Anode Propagating Shock Viewed through a Blue Filter	19

LIST OF FIGURES (Continued)

<u>Figure</u>		<u>Page</u>
14	Calculated Electron Density as a Function of Time for Two Predominant Ions, N_2^+ and N_4^+ , and Three Electron Temperatures	20
15	Schematic of the Microwave Interferometer, Waveguide Version	22
16	Plots of the Interferometer Signal as a Function of the Position of the Teflon Rod in the Discharge Tube (Squares), the Derivative of the Interferometer Signal, and a Gaussian Fit to the Derivative	23
17	Discharge Voltage (Top), Current (Center), and Microwave-Interferometer Signal (Bottom) for a 3-Torr, 60-mA Discharge in N_2	24
18	Logarithmic Display of the Global Discharge Current and the Local Electron-Density Decay for Three Shock Strengths. Data are the same as in Fig. 17. Computed electron-density decays are for a pressure of 6 Torr, a recombination coefficient $k_r=2 \times 10^{-6}$, and the following two parameter sets: a) (slower decay) $N_e=3 \times 10^9 \text{ cm}^{-3}$, $T_e=1 \text{ eV}$ and b) (faster decay) $N_e=10^{10} \text{ cm}^{-3}$, $T_e=2 \text{ eV}$	25
19	Schematic Diagram of the Experimental Apparatus. L1 is an aspherical lens; I1 and I2 are iris diaphragms; PH1 is a 200- μm pinhole; and PH2 and PH3 are 500- μm pinholes	26
20	Experimental Absorption Spectrum and Simulation of Metastable-He $2^3S_1 \rightarrow 2^3P_{0,1,2}$ Transitions in 1-Torr He at 2-mA Discharge Current. Solid line is the experimental spectrum, and the dotted curve is the simulation	28
21	Axial Profiles of the Line-Integrated Density of He 3S_1 for 1-, 2-, and 5-mA Discharge Currents. Position of the tube-diameter transition is 0 mm. Tube diameters are indicated in the figure	29
22	Axial Emission Profiles of 3D He Metastable for 1-, 2-, and 5-mA Discharge Currents. Position of the tube-diameter transition is 0 mm. Tube diameters are indicated in the figure	30
23	Triplet-Metastable-He Excitation and Ionization Rates. Data points are taken from Ref. 17, and the solid lines are extrapolations	32
24	Reduced-Electric-Field Axial Profiles in the Region of the Double Layer for 1-, 2-, and 5-mA Discharge Currents. a) Reduced Electric Field with the Cathode in the Larger Diameter Tube. b) Reduced Electric Field with the Anode in the Wider Tube Section. The tube-diameter transition is at 0 mm, and the negative axial positions are inside the smaller diameter tube	33

LIST OF FIGURES (Continued)

<u>Figure</u>		<u>Page</u>
25	H ₂ -N ₂ Discharge Voltage as a Function of Gas Mixture and Pulse Duration. H ₂ is the fractional flow of H ₂ in the H ₂ -N ₂ gas mixture	35
26	Determined Electric Field for the H ₂ -N ₂ Gas-Mixture Discharge. The gas pressure was 2.5 Torr, and the current was 250 mA. The pulse length is the duration of the discharge	36
27	H-Atom-Fluorescence Waveform for Various H ₂ -N ₂ Gas Mixtures. Waveform peak heights were adjusted to the same scale (100, 50, and 20% H ₂). The waveform with closed circles (S.L.) was recorded with the discharge off and the probe-laser scattering from a pin at the focal point of the PMT collection optics. The inset is a semi-log plot of the decay portion of the waveform. Except for the scattered-light line, the slopes of the lines for the different gas mixtures are the same within experimental uncertainty	37
28	Temporal Decay of H-Atom TALIF Signal for Different H ₂ -N ₂ Gas Mixtures for a Cell Pressure of 2.5 Torr and a 500-μs, 250-mA Discharge Pulse. The delay time is the time at which the H-atoms were measured after the discharge pulse was turned off	38
29	Temporal Decay of the H-Atom TALIF Signal for a 100% H ₂ , 2.5-Torr, 250-mA Discharge. The open circles represent the signal decay after the discharge pulse is turned off for a 200-μs pulse. The closed diamonds correspond to the relative signal levels of the H-atom, probed 20 μs after the discharge pulse is turned off for pulses of 200, 500, and 1000 μs	39
30	H _α Plasma Emission in a H ₂ Discharge for 100- and 1000-μs Discharge Pulses	40
31	Relative H-Atom TALIF Signal as a Function of the Discharge Pulse Duration. Discharge conditions are the same as in Fig. 25. Note that the signal for the 10-μ discharge pulse (bottom graph) has been multiplied by 5X to facilitate comparison with the 100-μ pulse signal	41
32	H-atom TALIF Signal Calibration for a H ₂ Discharge from a Power-Deposition Calculation. The relative TALIF signal and calculated H-atom density were normalized at 10 μs	43
33	Absolute H-atom Density as a Function of Discharge Pulse Length in a H ₂ -N ₂ Pulsed Discharge	43
34	Fractional H ₂ Dissociation as a Function of Discharge-Pulse Duration for Different Gas Mixtures in a H ₂ -N ₂ Discharge	44

LIST OF FIGURES (Continued)

<u>Figure</u>		<u>Page</u>
35	Temporal Evolution of H ₂ Vibrational Populations for 10% H ₂ in a H ₂ -N ₂ Discharge for Two Initial Vibrational Temperatures	45
26	Comparison of the Calculated Temporal Evolution of H ₂ , v = 4 and 5, Vibrational Populations for Two Initial Vibrational Temperatures with Experimental H-Atom Densities	46

PREFACE

This report describes tasks performed during the period 23 March 1998 – 1 June 2002 under Contract F33615-98-c-2806 by Dr. Peter Bletzinger, Dr. Michael Brown, Dr. James Williamson, Mr. Alan Forlines, Mr. Robert Knight, and Mr. Darryl Trump. The contract was administered by the Propulsion Directorate of the Air Force Research Laboratory at Wright-Patterson Air Force Base, OH, with Dr. Biswa N. Ganguly as Project Monitor.

SUMMARY

Advanced diagnostic techniques were applied for the characterization of non-equilibrium, molecular-gas-mixture plasmas to elucidate the fundamental physics and aerodynamics associated with non-equilibrium air plasmas and the plasma kinetics in molecular-gas-mixture discharges. Progress made during this research project is summarized below.

Shock Propagation in Plasmas

Low-Mach-number shock waves propagating through a low-pressure, non-equilibrium, positive-column gas discharge have been observed to experience dispersion and velocity changes. These effects will be shown to depend on discharge polarity. Optical and electrical measurements will be described which demonstrate further polarity-dependent effects in discharge light emission and changes in electrical properties. Using two types of probes, electrical measurements were made of both the global changes in the discharge voltage and current and in the time-resolved local-electric-field changes. The measured behavior of the discharge and the shock wave indicate very localized triple- or quadruple-layer electric sheaths associated with the propagating shock wave; these sheaths provide local enhanced ionization at the shock front, which can sustain the discharge--at least during the short shock-propagation time.

He-Metastable Density in a Double Layer

The axial-population-density profile of 2^3S_1 metastable He was measured in the double layer formed at an abrupt transition of the tube diameter in a positive column by diode-laser absorption spectroscopy. The axial profile was also measured for 3^3D metastable He from spatially resolved $3^3D \rightarrow 2^3P$ plasma emission. The triplet-metastable-density profiles were measured with discharge currents of 1, 2, and 5 mA at 1-Torr pressure for both polarity conditions: a) when the cathode end of the discharge is in the large-diameter tube and b) when the anode end of the discharge is in the large-diameter tube. The diode-laser absorption profiles show enhanced production of triplet metastable He 2^3S_1 in the double layer region as compared to that in the

unperturbed positive column (small diameter), with the magnitude being strongly dependent on the discharge polarity.

H-Atom Measurement in a H₂-N₂ Pulsed Glow Discharge

The absolute concentration of hydrogen atoms was measured in the positive column of a pulsed dc discharge by two-photon-absorption laser-induced fluorescence (TALIF) in H₂ and H₂-N₂ gas mixtures at constant pressure and current. The discharge pulse duration was varied from 10 μ s to 1 ms. For shorter pulse durations of 10 and 100 μ s, the H-atom signal decreased monotonically with H₂ concentration; for longer pulse durations of ≥ 500 μ s, the fractional dissociation of the H₂ was enhanced with increasing N₂ concentration. Temporally resolved H-atom-concentration measurements were made to determine the change in H-atom production from direct-electron-impact dissociation of H₂ at short times compared to that from multi-quantum vibrational-energy-transfer-induced dissociation of H₂ at long times.

INTRODUCTION

Non-equilibrium air plasmas play a significant role in modifying the properties of many processes crucial to Air-Force interests. Quantitative information on the ionization and dissociation characteristics of non-equilibrium glow discharges in air and air mixtures is relevant to rocket re-entry and boost phase, combustion signatures, laser spikes, plasma cloaking, enhanced corrosion, ignition of aircraft and missile engines, and aerodynamic drag and shock-wave reduction. It is imperative that non-equilibrium air plasmas be studied with advanced diagnostic techniques to aid the understanding of the fundamental physics and fluid dynamics of these important systems.

While the physics and aerodynamics of shock-wave propagation under thermodynamic-equilibrium conditions have been studied extensively with regard to problems concerning spacecraft re-entry and hypersonic flight, the effects of non-equilibrium conditions have only recently been examined. The fluid-dynamic behavior of a non-equilibrium gas is characterized by two features that distinguish it from an equilibrium gas. First, the hydrodynamic movement,

such as shock-wave propagation, couples energy between the internal and the translation modes. Since the internal energy distribution in the non-equilibrium air plasma under conditions of external electrical excitation is significantly different from that in the translational mode, the energy coupling with a positive feedback can transfer energy very efficiently from one mode to another. An example of this is the enhancement in ionization in a weakly ionized gas at the expense of shock-wave attenuation. Second, the degree of non-equilibrium can affect the intensity of heat loss and energy pumping, which determines the non-equilibrium storage of energy in the internal modes of the gas (vibrational, electronic, and ionization). The joint action of these two factors can lead to the appearance of new effects--namely, anomalous dispersion and enhanced attenuation of shock waves. The exact mechanisms responsible for these new effects in weakly ionized non-equilibrium plasmas, however, are not well understood.

In recent years a number of Russian studies have been published on the experimental investigation of the propagation of shock waves in non-equilibrium gases.¹⁻⁸ In these studies it was noted that for weakly ionized gases, the propagation of shock waves displayed certain anomalous behavior--namely, 1) a reduction in the pressure discontinuity at the shock front, 2) an increase in the velocity and amplitude of acoustic waves within the ionized-gas region (i.e., an apparent increase in the velocity of sound), and 3) a reduction in drag on spherical bodies, although primarily at lower velocities. For example, Kilmov, *et al.*¹ studied the intensity (i.e., density vs. time record) of a shock wave (generated in a shock tube) traveling in the cold plasma of an unsteady glow discharge in air. They found that as the shock wave moves into the plasma, it undergoes a transformation, which includes the splitting of the shock into two waves--a so-called precursor wave and a residual shock wave. Whereas the velocity of the shock wave was 1400 m/s, the velocity of the precursor wave was 1560 m/s; that is, the two waves separated as they moved through the plasma. Furthermore, these investigators reported that the shock wave was spatially broadened by a factor of ~ 10 , as compared to a shock in unionized air. In addition to the precursor and residual waves, these authors observed another anomalous feature--a low-density region (30% below that of the pre-shock gases) that precedes the precursor wave and which they refer to as the leader wave.

WORK ACCOMPLISHED

Shockwave Propagation in Plasmas

Initially, previous results from this laboratory were reviewed to obtain a better understanding of the physics of shockwave propagation in plasmas. Quite early it was observed that while the shockwave was propagating in the discharge plasma, its velocity increased--which was a clear indication that this effect could not be explained by a thermal gradient in the discharge or at the interface between plasma and neutral gas. To investigate the thermal properties further, an equation describing the relation between the Mach numbers on both sides of a temperature jump in a shockwave-propagation path and the temperatures on the two sides⁹ was used to verify our experimental results:

$$\begin{aligned} & \frac{2}{\gamma_1+1} M_1 \left(1 - \frac{1}{M_1^2}\right) + \frac{2}{\gamma_1-1} \left\{ \frac{[2\gamma_1 M_1^2 - (\gamma_1-1)][(\gamma_1-1)M_1^2 + 2]}{(\gamma_1+1)^2 M_1^2} \right\}^{\frac{1}{2}} \\ & * \left[1 - \left\{ \frac{\frac{2\gamma_2}{\gamma_2+1} M_2^2 - \frac{\gamma_2-1}{\gamma_2+1}}{\frac{2\gamma_1}{\gamma_1+1} M_1^2 - \frac{\gamma_1-1}{\gamma_1+1}} \right\}^{\frac{\gamma_1-1}{2\gamma_1}} \right] = \frac{2}{\gamma_2+1} \sqrt{\frac{T_2}{T_1}} M_2 \left(1 - \frac{1}{M_2^2}\right) \end{aligned} \quad (1)$$

where M_1 and M_2 are the Mach numbers in the two temperature zones; $\gamma = (N+2)/N$, with N being the number of degrees of freedom of the atoms or molecules; and T_1 and T_2 are the gas temperatures. For our case we assume that T_1 = room temperature and $\gamma_1 = \gamma_2 = 1.4$. Also we can relate the velocity in the hot gas to the Mach number in the hot gas:

$$V_2 = M_2 * 343 \text{ (m/sec)} * \sqrt{\frac{T_2}{T_1}} \quad (2)$$

The velocities were measured at two positions in a discharge using the setup shown in Fig. 1. From the difference in time of arrival between each laser pair, the velocity at each position can be calculated. An example of the laser signals is shown in Fig. 2. From the measured velocities for cold gas and for propagation in the plasma, the temperature in the plasma can be obtained as

Schematic of Experiment

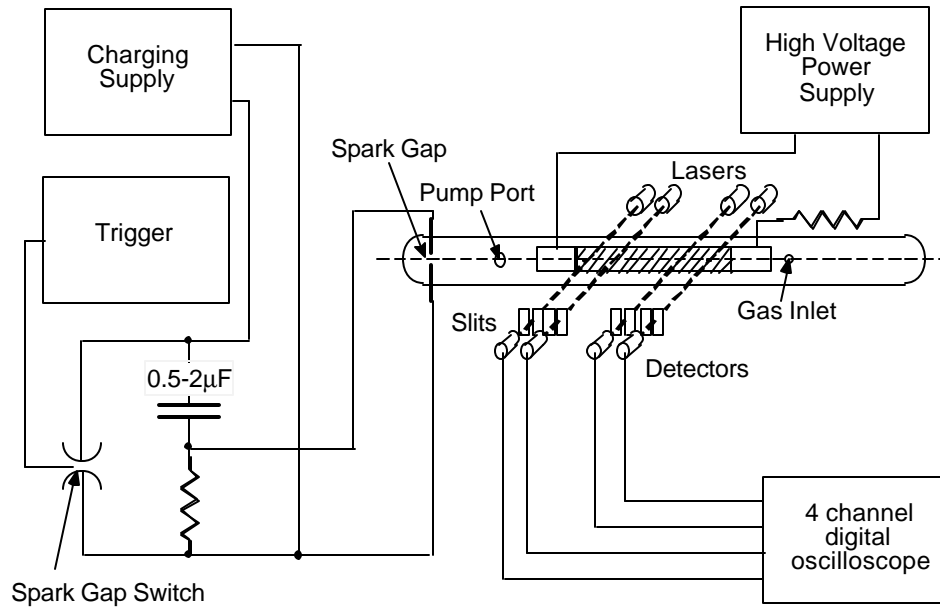


Figure 1. Experimental Setup for Measuring the Local Velocity at Two Positions in the Positive Column of a Gas Discharge.

well as the corresponding Mach number. The equation is implicit, and solutions are obtained by first obtaining a Mach number for an assumed temperature (Iteration 1) and then comparing the computed velocity with the measured velocity (Iteration 2) until a match is obtained. The results for a discharge in 15-Torr N_2 are shown in Table 1.

While the temperatures at Position 1 are reasonable, a calculated temperature difference of up to 230 deg is present between Positions 1 and 2--clearly not possible in a uniform positive column for two positions separated by 129 mm. This calculation also shows that the observed phenomena cannot be caused by thermal effects only.

An interesting facet of the propagation of shock waves in a gas discharge is the behavior of the discharge itself. It was noticed early in this investigation that the optical radiation of the discharge was disturbed by the shock wave. This effect must be distinguished from the influence of the spark-gap/shock-wave generator itself. The spark gap emits copious amounts of vacuum UV, which generates sizable amounts of ionization (we measured photon-generated currents in the tens of milliamps). However, this current pulse or enhanced ionization is short and its effects negligible

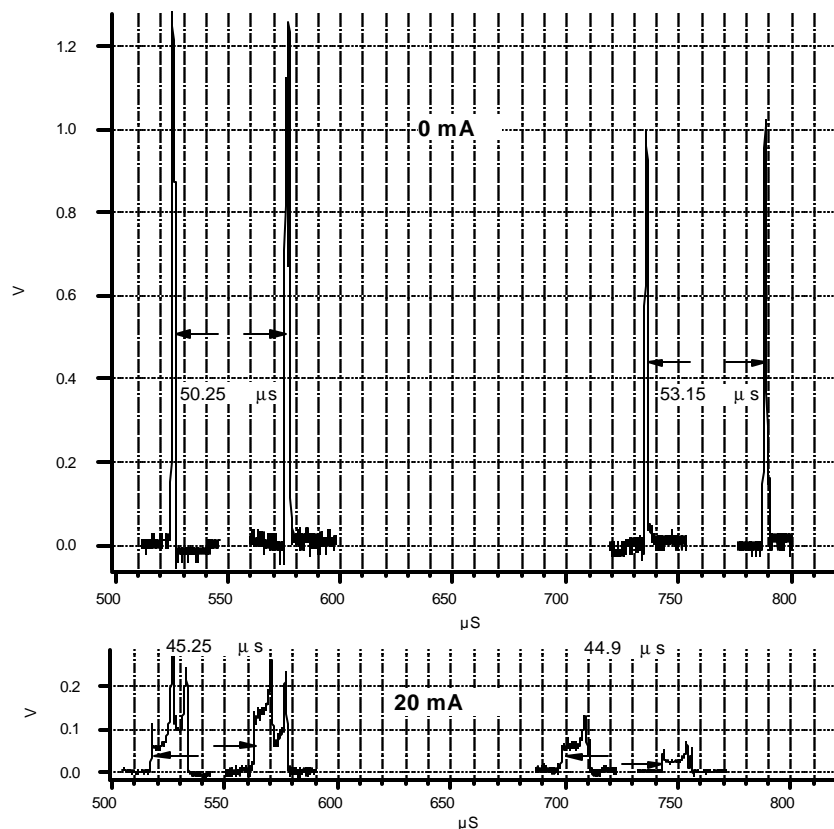


Figure 2. Laser Signals at Positions 40 and 169 mm from the Cathode in 15-Torr N_2 . Note not only that the velocities are increasing in the discharge but also that the velocity at the downstream position, while lower in neutral gas, becomes higher than the upstream velocity when the discharge is on.

Table 1
Results for 15-Torr N_2

Discharge Current (mA)	Velocity Pos. 1 (m/s)	Mach No. Pos. 1	Temperature Pos. 1 (K)	Velocity Pos. 2 (m/s)	Mach No. Pos. 2	Temperature Pos. 2 (K)
0	514.5	1.5	300	487.4	1.421	300
20	577.1	1.459	399.1	581.9	1.37	460
30	613.5	1.437	464.5	609.9	1.357	515.1
40	642.8	1.421	521.5	644.9	1.342	589.1
50	653.3	1.416	542.8	722.0	1.312	772.3

when the shock wave propagates into the discharge. Also, this effect was reduced by inserting a tubing bend between the spark gap and the discharge tube.

To better understand the optical-emission characteristics of the shock wave in the discharge, a < 1 -mm-wide portion of the discharge axis was imaged on a photomultiplier tube using a vertical slit. The spectral response was controlled by a narrow-band filter (337.1 nm for the 0-0 transition of the N_2 second-positive system), and the photomultiplier time response was determined using a ≤ 1 -k Ω load resistor. Digital filtering was used to reduce the noise in the light signal. The measurements were performed at four positions along the 200-mm-long discharge, and the time of arrival of the shock wave was recorded by a separate laser-photodeflection station at the same axial position. Figure 3 shows measured photomultiplier signals at a discharge current of 100 mA in 10 Torr of N_2 and a pulse energy of 144 J. The solid lines represent data with the discharge cathode near the spark gap (Case C); the dashed lines indicate results with the anode near the spark gap (Case A). The distances from the upstream electrode are as indicated in Fig. 3. The measurements very near the up-stream electrode (8 mm) differ from the other measurements in the positive column of the discharge. In Case A, a very large light pulse was measured, while for Case C a much smaller--but also increasing--signal was measured. It appears that the light emission in this region remains on for the entire measurement time. From a point 30 mm into the positive column, in Case C the signal decreases at the exact moment of shock-wave arrival and with a very sharp fall time. In contrast, for Case A the signal begins to decrease from the moment the shock enters the positive column; the decrease is relatively gradual and not correlated with the arrival time of the shock wave. The decrease in luminosity is almost zero, i.e., the discharge has been almost extinguished temporarily [this corresponds to the decrease in electron density observed in the microwave-interferometer measurement (discussed below)]. Later, at random intervals, light peaks appear when the discharge attempts to switch back on (as also observed for the electron density in the microwave measurements). The laser signals signifying the arrival of the shock wave indicate timing differences for the two cases; only a small part of this difference may be ascribed to jitter in the measurements. For Case A the shock wave consistently arrives later, and the shock-wave speed is lower. Note that it is the front of the (dispersed) laser signal that correlates with the light signal for Case C.

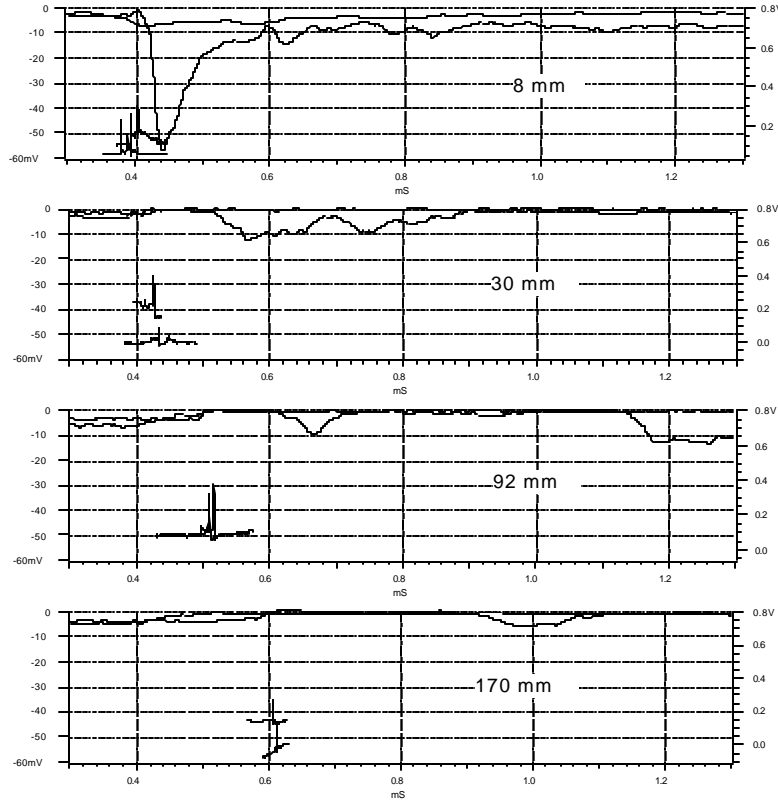


Figure 3. Top - 337.1-nm Spatially Resolved Light Emission at a Location 36 mm from the Upstream Electrode and Laser-Photodeflection Signals; Middle - Discharge Voltages; Bottom - Discharge Currents for Case C (Solid Lines) and Case A (Dashed Lines). The two vertical lines indicate the time of arrival of the shock wave at the discharge and at the 36-mm measuring location, respectively.

Because of the differences between Case A and Case C, measurements were also made of the discharge current and voltage using a low-inductance current-measuring resistor and a high-voltage probe. It is, of course, understood that the voltage and current measurements are global and cannot be correlated with the local shock-wave position, except when the shock wave enters the plasma. Figure 4 displays the results of measurements of the 337.1-nm light emission (top), the discharge voltage (middle), and discharge current (bottom). Again, the solid curves are for Case C, and the dashed curves are for Case A. The polarity of the voltage and current curves is shown in inverted form for Case C. The light measurement was made 36 mm from the upstream electrode; the discharge conditions were the same as those in Fig. 3. It is obvious that the two polarity cases exhibit quite different behavior with regard to current and voltage. For Case C

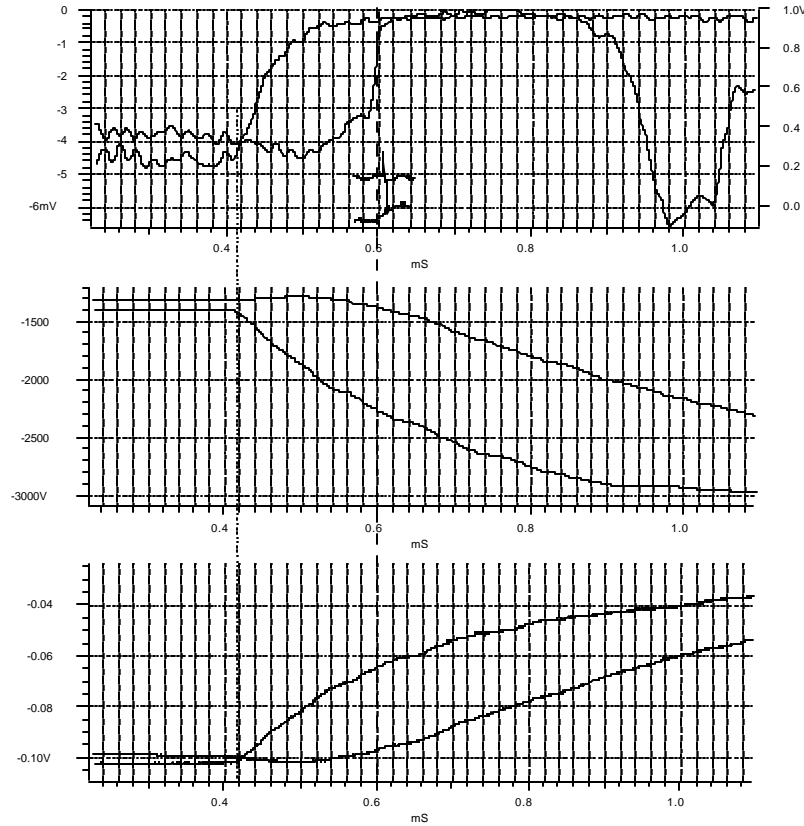


Figure 4. 337.1-nm, Spatially Resolved Light Emission Measured at Four Positions from the Electrode Nearest the Spark Source. Also shown are the laser-photo-deflection signals at the same position. Solid lines - Case C; dashed lines - Case A.

initially the discharge impedance decreases since the voltage decreases while the current increases. After only about 100 μ s, the impedance increases with increasing voltage and decreasing current. For Case A the impedance increases immediately upon entrance of the shock wave into the plasma. The exact shape of the impedance increase (discharge switching off) at later times is also determined by the unknown regulating characteristics of the current-controlled power supply; therefore, definite statements concerning the discharge behavior for times later than 1 ms after shock-wave initiation cannot be made. It appears, however, that sizeable plasma conductivity is still present milliseconds after shock-wave initiation-again correlating with our electron-density measurements.

The most important finding from these measurements is that the discharge behavior is very different for the two polarities. It is quite obvious that the influence of the discharge on the

shock wave is dependent on the direction of the electric field and--even more important--that the observed dispersion and velocity change of the shock wave in the discharge are, at least in part, caused by electric-field effects. Apparently in Case C where the cathode-fall region is exposed to the initially undispersed shock wave, ionization is enhanced for $\sim 200 \mu\text{s}$. Although this does not hold for Case A, excitation is enhanced and is restricted to the anode region, as shown by the very large increase in emission. The most significant effect in both cases is the almost complete extinction of the positive column. To date, no explanation for these observations has been found.

A double discharge tube was used to study the influence of a shock wave on a discharge when the shock wave has already been modified by a previous discharge. The optical and electrical diagnostics were the same as those employed in the previously reported experiment. The discharge tube (dimensions shown in Fig. 6) was very short, and it quickly became apparent that the spacing was too small to allow a positive column to develop at the pressures used (the laser and photomultiplier were located 23 mm from the center electrode). Therefore, the optical emission from the discharge was significantly reduced, and the signal-to-noise ratio was too small to permit the measurement of small changes in emission. Also the travel time in the discharge was too short to permit observation of the smaller changes in emission before arrival of the shock wave. The only signals that were observed with some degree of accuracy were the large increases in emission upon re-ignition of the discharge after the shock wave had passed through. The only useful signals were the changes in anode voltage caused by the shock wave.

Figure 5 shows the anode voltages of the second discharge for 5- and 12-kV capacitor voltage, with the first discharge off and 50- and 100-mA current. The assignments of the three electrodes were as follows: cathode - anode - cathode. It can be seen that when the first discharge is operating, the change in the anode voltage of the second discharge is reduced, with the rate of reduction increasing with first discharge current. The initial decrease before shock-wave arrival for the cathode-upstream case (observed previously) is absent as a result of the short discharge length. Figure 6 is a plot of the increase in percent of the discharge voltage caused by the shock wave for two capacitor voltages at various pressures. While the increase in discharge voltage is much greater for the higher shock-wave energy, the influence of the first discharge is stronger at the lower shock-wave energy.

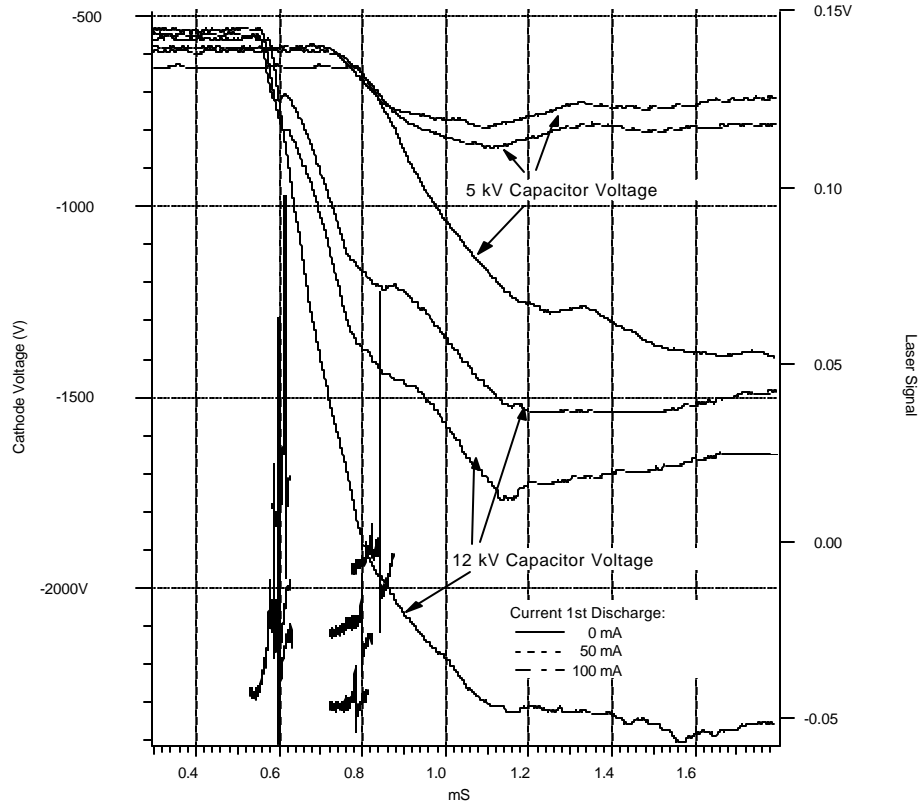


Figure 5. Discharge Voltages of the Second Discharge at a Second-Discharge Current of 100 mA, a Pressure 40-Torr N₂ at Two Spark-Gap Capacitor Voltages, and Various Currents of the First Discharge.

It was noted earlier that the shock-wave propagation in the direction anode-cathode (Case A) was slower than in the opposite direction (Case C). This polarity dependence was investigated using optical and probe methods. The optical setup was the same as that used for previous spatially and temporally resolved 337.1-nm emission measurements. Figure 7 shows results from measurements of discharge voltage, discharge current, and 337.1-nm sidelight emission. The global characteristics of the discharge current and discharge voltage differ for the two polarities, as previously noted. Remarkably, the local characteristics of 337.1-nm emission also differ—but in another way. A change in emission occurs when the shock wave enters the discharge—for Case A the emission gradually decreases as the shock progresses; for the opposite polarity (Case C), the emission increases. As the shock arrives at the photomultiplier location, the emission becomes almost zero in both cases. Note that for Case A, the arrival time is slightly later than for Case C, in accordance with the previous observations. The sudden decrease in emission upon

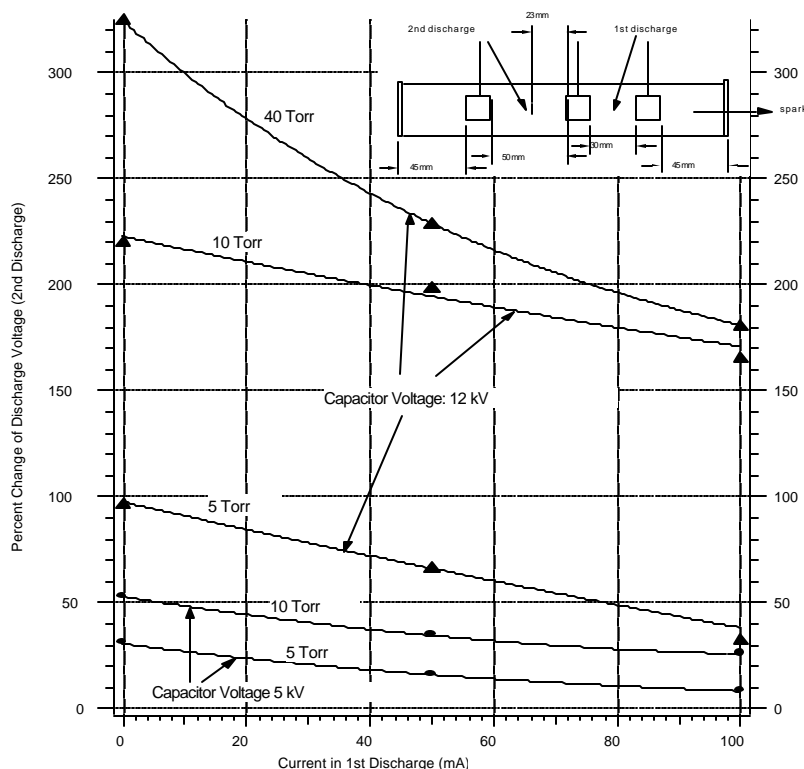


Figure 6. Change of the Second-Discharge Voltage (in Percent) as a Function of the First-Discharge Current and the Spark-Gap Capacitor Voltage.

arrival of the shock wave at the observation point can be explained quite easily by the fact that behind the shock wave, at a velocity of \sim Mach 1.7, the neutral density n increases by a factor of three, which greatly decreases the normalized electrical field (E/n)--even for a slight increase in E . This large decrease in E/n causes a very large decrease in electronic excitation, given the exponential dependence of the electron-excitation cross sections on E/n . The variations in the 337.1-nm emission before arrival of the shock wave seem to indicate an increase in electric field for Case C and a decrease for Case A. Note that these local variations of E are opposite to the global changes in discharge voltage.

To gain further insight into these rather complex relationships, a discharge tube with two electric probes, separated along the tube axis by 2 cm, was used to measure local floating potentials. The probes were placed several millimeters radially into the discharge region to avoid measuring

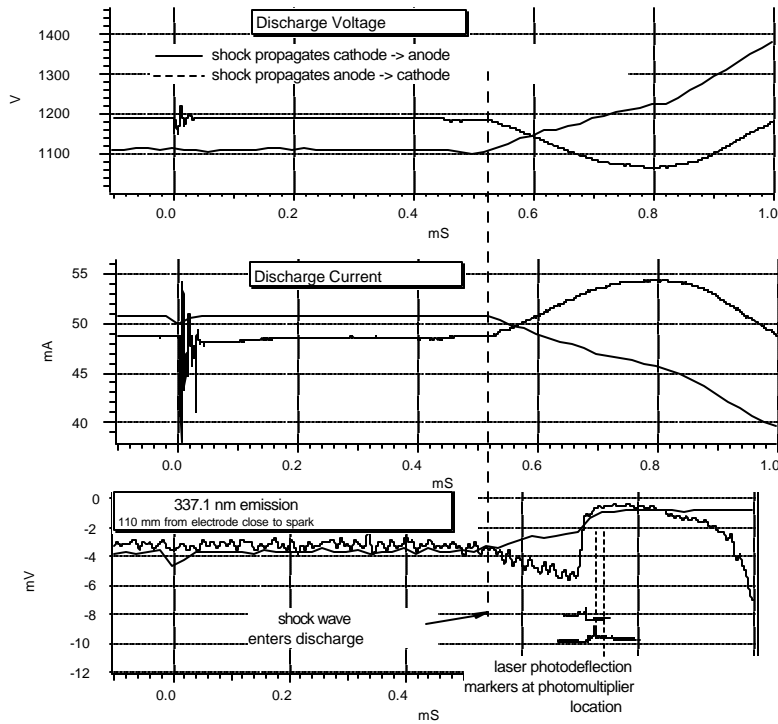


Figure 7. Discharge Voltage and Current and 337.1-nm Sidelight Emission for a 5-Torr, 50-mA Discharge in N_2 ; 5 kV at 2- μ F Spark Discharge.

only the wall potential. Floating-probe measurements are limited by the fact that the probes must not disturb the discharge by drawing a large current, i.e., the probes must be small. Drawing a small (ion) current means that their source impedance for the floating-voltage measurement is large (when the floating probes were loaded with one and two high-voltage probes with an input resistance of 100 $M\Omega$, this impedance was estimated to be 40 $M\Omega$). This means, in turn, that even a 100- $M\Omega$ high-voltage probe will cause an almost 30% error in the measured floating voltage. In addition, at these impedances the normal high-voltage-probe capacitance will limit the minimum measurable rise-time to 100 μ s. Also the separation of 2 cm will result in additional distortion of the fast-shock-wave signal if one uses the difference in the two probe signals to measure the electric field between the two probes.

Figure 8 displays the results of floating-probe measurements for 5-Torr N_2 at a 60-mA discharge current. The laser-deflection signals are for the locations in the center between the probes and at the edge of the downstream electrode. The floating-probe voltages follow the discharge voltage

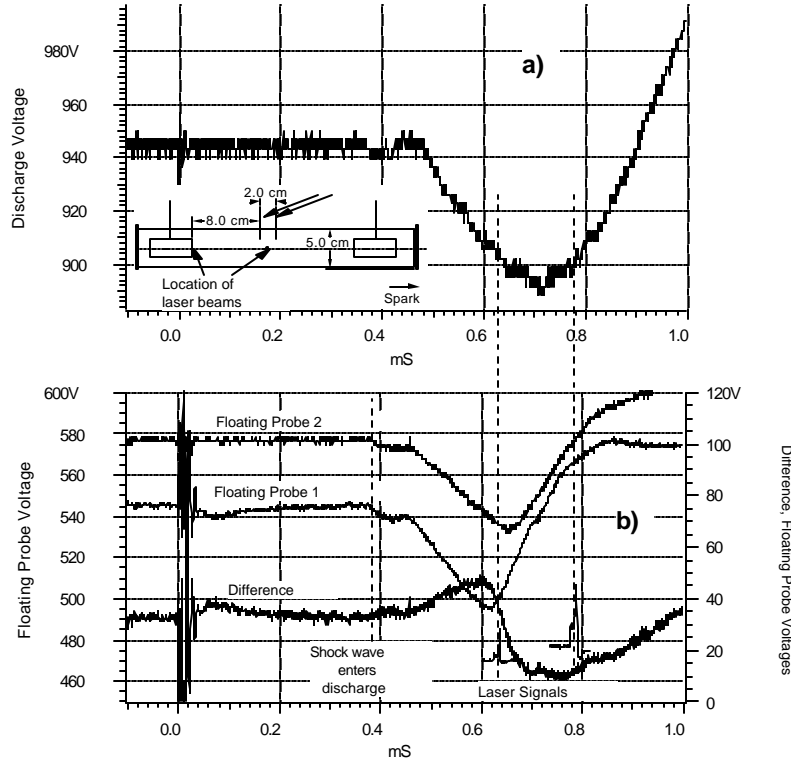


Figure 8. Discharge Voltage (Top), Floating-Probe Voltages and Their Difference (Bottom) for a Cathode-to-Anode Directed Shock Wave in 5-Torr N_2 at 60-mA Discharge Current.

until the arrival of the shock wave and then rise sharply, the rise probably being limited by the factors mentioned above. It is obvious that a fast local change in voltage occurs upon arrival of the shock wave, indicating that an electric field is associated with the shock front. Note that before the shock wave arrives, the voltage between the probes increases, in agreement with the assumption of a slow increase in the electric field based on the emission data. The probe-voltage difference decreases rapidly as the shock wave passes through the observation region. Figure 8 is for Case C. For Case A the difference in voltage decreases before arrival of the shock, again in accordance with the emission data, and also decreases rapidly when the shock wave passes through the observation region.

As mentioned previously, the emission data after the shock wave passes through the observation region can be explained, but the behavior prior to this time requires further study. One puzzling aspect is the fact that the discharge current does not vary significantly during the time when the

shock wave is passing through the discharge (Fig. 7), even though it is claimed that because of the rapid decrease in E/n , the electron excitation-and, therefore, the electron ionization-is reduced considerably. This reduction may require the generation of an abundance of electrons in the shock wave which, while the electron temperature decreases rapidly, must still provide current continuity.

To this point the electric-field changes caused by the shock wave propagating in the discharge were determined by electrical wire probes that penetrated into the discharge and measured the signals with 100-M Ω -input-resistance high-voltage probes. On closer investigation, with the high-voltage probes representing a 100-M Ω load to ground, it was determined that the plasma-source impedance under these conditions was ~ 40 M Ω . While this causes an error in the floating-voltage measurement, the more serious consequence is a very long time constant of ~ 90 μ s due to the non-negligible circuit capacitance. This time constant is, of course, much longer than the electric-field change caused by the shock wave passing by the probes. An alternative method where two parallel copper rings are wrapped around the discharge tube was then investigated. It was calibrated using a pair of opposed electrodes in a glass tube, which were connected to a pulsed voltage of 1-kV amplitude. The measured high-voltage pulse at the electrodes is negative going and has a faster risetime. The spatial resolution of the differential probe was tested also, and it was limited; at a 10-mm displacement from the center of the electrode gap, the measured voltage was 10% of the voltage with the probe directly in the center of the gap. While the differential-probe spatial resolution is insufficient to resolve the shock-wave structure, its response time is faster than that of the floating-point voltage probes. In Fig. 9 the signals from the floating probe, differential probe, and 337.1-nm photomultiplier are compared. The differential probe has a faster response time for the shock-induced electrical-field change, but its spatial resolution still limits the time response. The fastest response is from the 337.1-nm signal. It is important to note that all three methods have the same basic response: slow growth (cathode - anode direction) or decrease (anode-cathode direction) in electrical field/337.1-nm emission when the shock enters the discharge and a sharp decrease when the shock passes the observation point. The differential-probe response changes in shape but not in basic features for different locations along the positive column, as shown in Fig. 10.

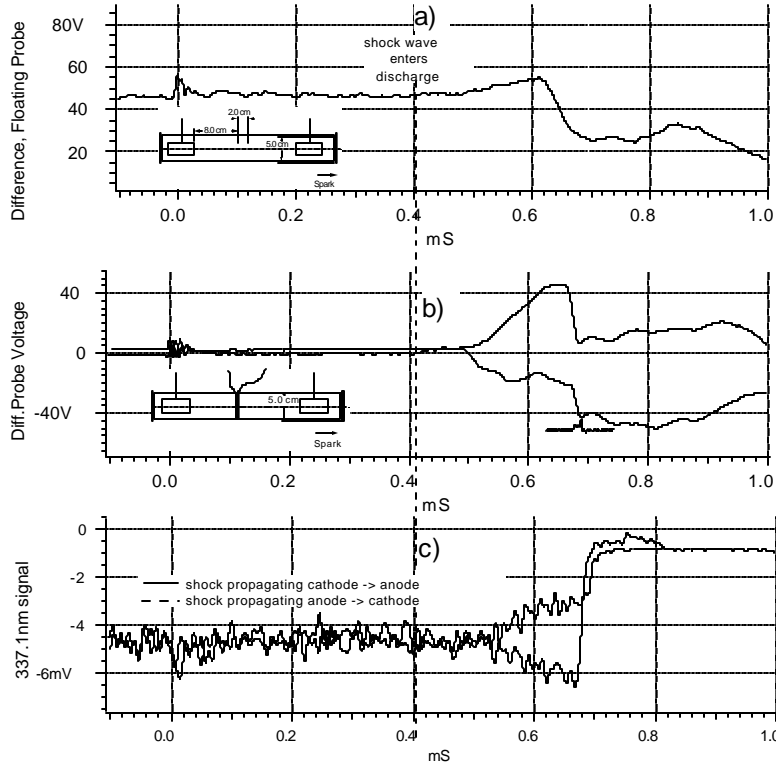


Figure 9. Comparison of a) Difference in Floating-Probe Voltages, b) Differential-Probe Output, and c) 337.1-nm Collimated Sidelight Emission.

A gateable CCD camera with a 1.2- μ s exposure time was used to obtain time-resolved images of the discharge as the shock wave propagated through it. Figure 11 contains a sequence of images for a shock propagating from cathode to anode. This sequence had no spectral resolution; therefore, the nitrogen afterglow is still visible as it fills the discharge volume, but the more intense boundary of the active discharge can clearly be observed to recede, as indicated by the dashed line. In Fig. 12 a sequence for anode-to-cathode shock propagation is shown. The shock is less clearly defined but still visible during propagation. At later times in the sequence, the discharge can be seen in the initial stages of re-ignition. Using a blue band-pass optical filter, we eliminated most of the long-lived radiation, sacrificing signal-to-noise ratio. A cathode-to-anode shock sequence is shown in Fig. 13. The shock front is much more clearly defined and also appears to be flatter. Re-ignition is also shown; here, it appears to begin in the center of the discharge.

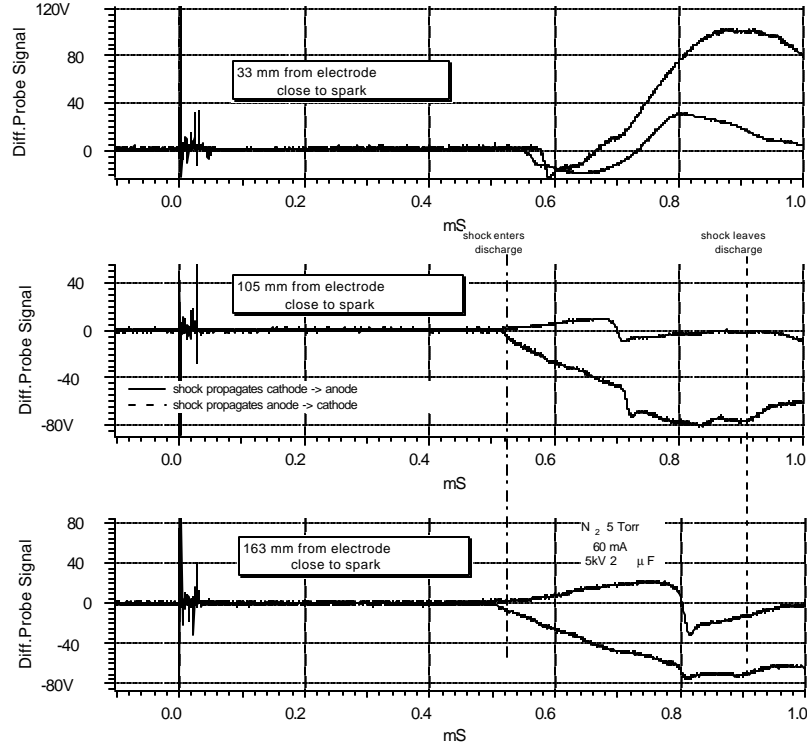
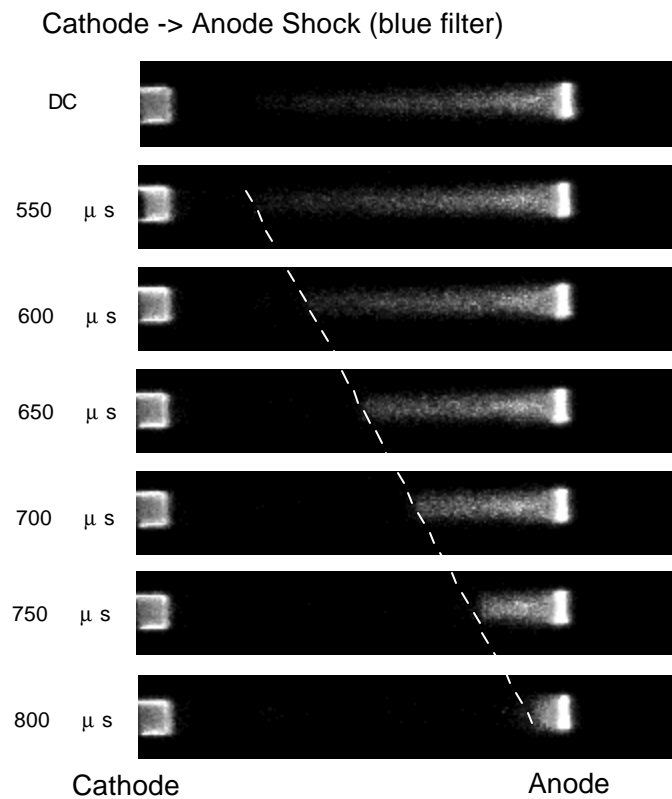


Figure 10. Differential Probe Output at Three Locations along the Discharge.

A striking feature of these sequences is that neither the anode nor the cathode glow seems to change during the shock traversal. Only at times later than ~ 1 ms does the anode glow appear to become thinner, indicating that the discharge current remains approximately constant—at least during the shock-traversal time. This observation is in agreement with the time-resolved discharge-current measurements that show a current deviation of only $\sim 10\%$ from the dc value during this time (increasing for the cathode-anode direction and decreasing for the anode-cathode direction). Since the CCD camera images as well as the previous time-resolved sidelight-emission measurements indicate an extinction of radiation after passage of the shock, it can be assumed that volume ionization in the space behind the shock will also cease. On the other hand, with the discharge current only slightly affected, the discharge conductivity must remain approximately constant (the discharge voltage also changes only by $\sim 10\%$). Therefore, the electron-density decay was investigated more closely.



pulse3[99/7]Photo6July/C/Acx

Figure 11. Images for a Cathode-to-Anode Propagating Shock.

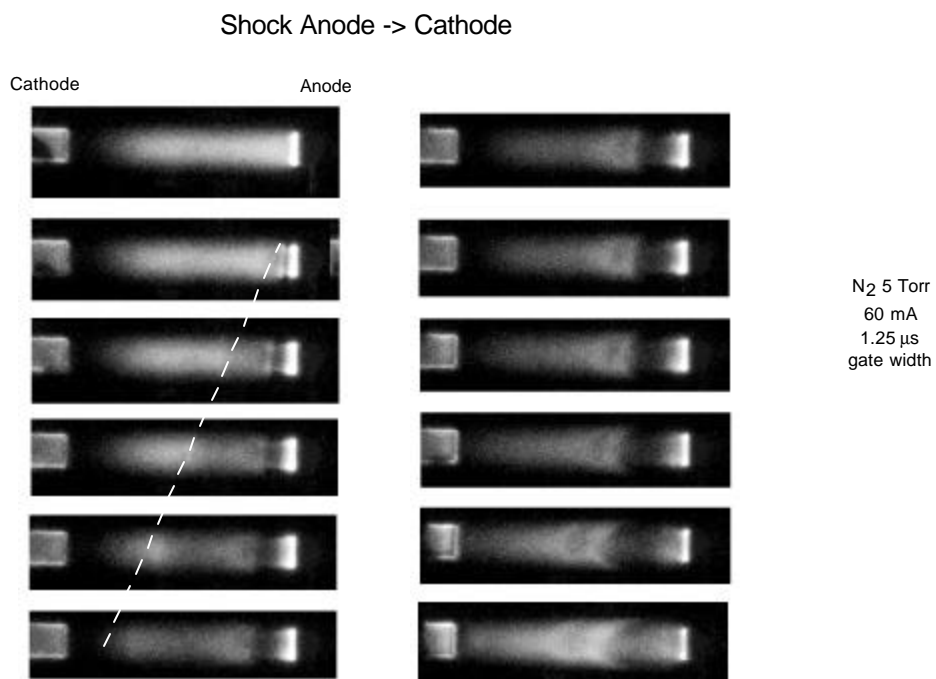


Figure 12. Images for an Anode-to-Cathode Propagating Shock.

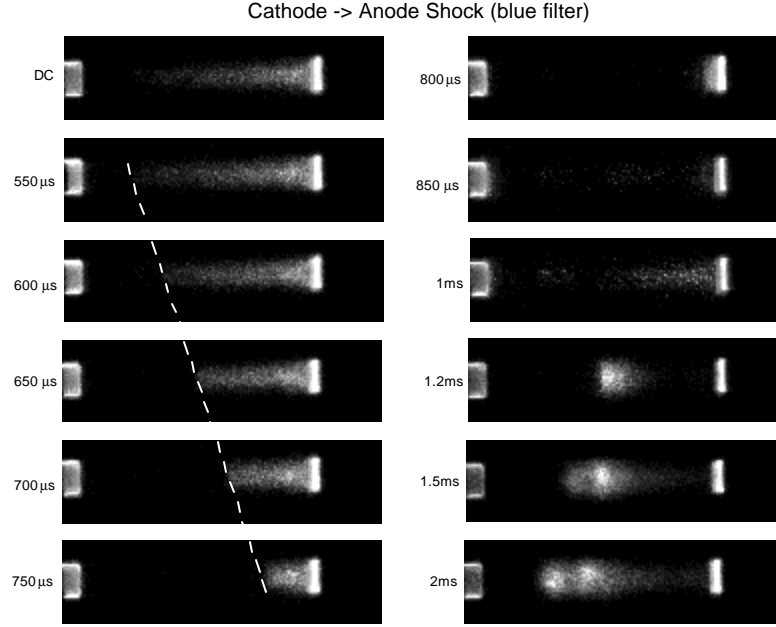


Figure 13. Images for a Cathode-to-Anode Propagating Shock Viewed through a Blue Filter.

For the current discharge conditions, the electron-density loss will occur predominantly by recombination and ambipolar radial diffusion to the wall. The electron-continuity equation for the decaying plasma is then

$$dn_e/dt = -k_r n_e^2 - n_e/T_d \quad (3)$$

where k_r is the recombination rate and T_d the ambipolar-diffusion time constant. Obtaining $E/n = 2 \times 10^{-16} \text{ Vcm}^2$ from electric-field measurements with the electrical probes at a pressure of 5 Torr, the electron drift velocity in nitrogen is determined to be $3 \times 10^6 \text{ cm/s}$. At 4.8-mA/cm^2 discharge-current density (100-mA current), this results in an estimated electron density, n_{e0} , before the shock arrival of 10^{10} cm^{-3} . The recombination coefficient k_r is a function of the electron temperature T_e : $k_r = f(T_e)^{k_1}$, where the value of k_1 has been given by various authors as being between - 0.5 and - 1.5. The time constant for ambipolar diffusion is inversely proportional to T_e . In the absence of an applied electric field, T_e rapidly decreases to 0.3 eV; this lower limit is set by the vibrational temperature, which will decay much more slowly. Figure 14 shows the calculated decays of n_e for a predominant ion N_2^+ ($k_r = 2 \times 10^{-7}$) or N_4^+ ($k_r = 2 \times 10^{-6}$)

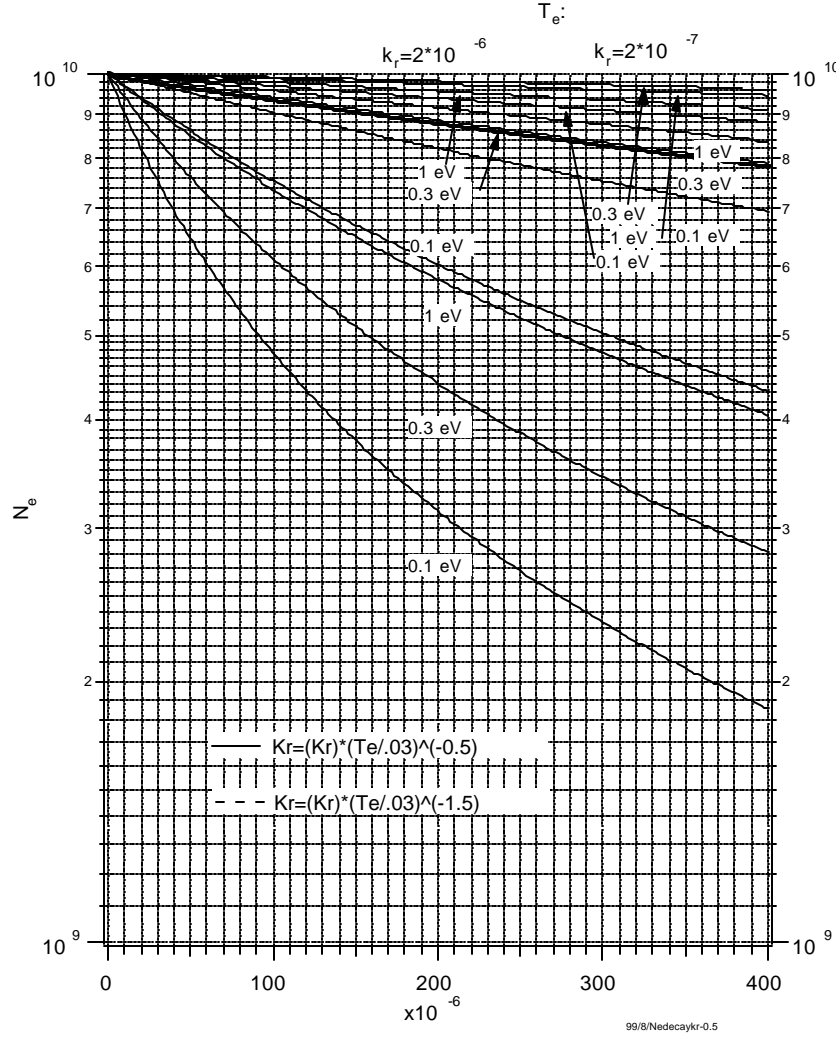


Figure 14. Calculated Electron Density as a Function of Time for Two Predominant Ions, N_2^+ and N_4^+ , and Three Electron Temperatures.

and for electron temperatures of 0.1, 0.3, and 1 eV. The solid lines are for an exponent of - 0.5 and the dashed lines for an exponent of - 1.5.

The neutral density increases by a factor of 2.2 for Mach 1.7 after the shock; then, at a maximum traversal time of 400 μs , n_e will have decreased by 4% or 21%, using a T_e of 0.3 eV and an exponent of - 1.5, depending on whether the predominant ion is taken to be N_2^+ or N_4^+ . This relatively moderate decrease in n_e is the consequence of assuming a value for T_e that is considerably above room temperature but lower than the expected T_e in the presence of an applied electric field. The long decay time of n_e has been observed in microwave-interferometry

measurements that are described below. This maximum decrease of n_e may be consistent with the observed decrease in current for the anode-to-cathode direction; it is inconsistent with the current increase for the cathode-to-anode direction, where the current actually increases during the shock traversal time. Even more important, with a neutral-density increase by a factor of 2.2 after the passage of the shock, the resultant drop in E/n will reduce the drift velocity to 1.5×10^6 cm/s. For maintaining approximately the same discharge current, n_e must increase by at least a factor of two!

Time-resolved electron density was measured using a microwave interferometer with an 8-GHz solid-state source and a focusing-mirror arrangement designed by Prof. J. Verdeyen of the University of Illinois. The mirror and discharge-tube setup are shown in Fig. 15. It is expected that the mirror pair, illuminated by the two horn antennas, will have a focusing volume of ~ 3 -4 cm, corresponding roughly to one wavelength. The resolution was tested by inserting a Teflon rod into the discharge tube and moving it across the focus of the mirrors. The measured interferometer response is shown in Fig. 16 (squares). Also shown is the derivative of the signal, corresponding to the actual resolution, and a Gaussian fit to the derivative from which a full-width at half-maximum value of 4 cm was obtained. This confirms good alignment of the mirrors and the discharge tube. Since the differential signal from the interferometer was only on the order of a few millivolts (4-5 mV)--a level insufficient to permit recording on a digital oscilloscope--a differential amplifier with a bandwidth of > 1 MHz was constructed.

Measurements of the discharge voltage, current, and microwave-interferometer signal are shown in Fig. 17 for three energy-storage voltages and for shock propagation from anode to cathode. The laser-photo-deflection signals (bottom, lower diagram) indicate the time at which the shock passes through the center of the interferometer focal volume. As observed previously for anode-to-cathode propagation, the discharge voltage increases immediately when the shock wave enters the discharge; the discharge current also decreases immediately, approaching zero. With increasing shock strength, the voltage increase (current decrease) accelerates. The interferometer signals indicate a large increase of electron density upon shock arrival; for the fastest shock wave, the electron density increases by a factor of ~ 2.2 and then rapidly decays to zero. Regarding the global discharge voltage and current, the rate of change in local electron density

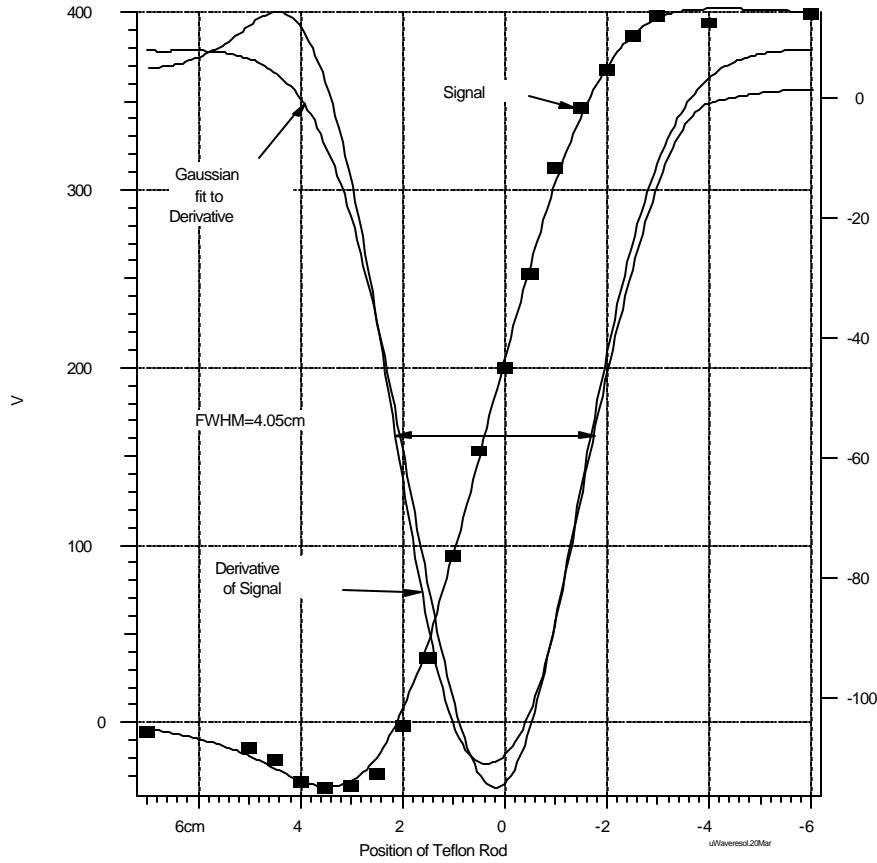


Figure 16. Plots of the Interferometer Signal as a Function of the Position of the Teflon Rod in the Discharge Tube (Squares), the Derivative of the Interferometer Signal, and a Gaussian Fit to the Derivative.

strengths the (local) electron-density decay is faster than the (global) current decay. Normally, one would expect that during the decay, since the reduced electric-field E/n decreases, the drift velocity would also decrease. This would cause the current decay to be faster than the electron-density decay. It is known that the discharge voltage--and, therefore, the E/n --decreases during the decay of current and electron density. One hypothesis is that the displacement current caused by the space charge associated with and propagating with the shock front is additive with the discharge current. The problem with this hypothesis is that in order to increase the decaying discharge current when traveling from anode to cathode, the space charge would have to be positive.

Previously a simple model was used to compute the electron-density decay in a tubular discharge due to volume recombination and diffusion losses to the wall¹⁰ (see Fig 14). Assuming a

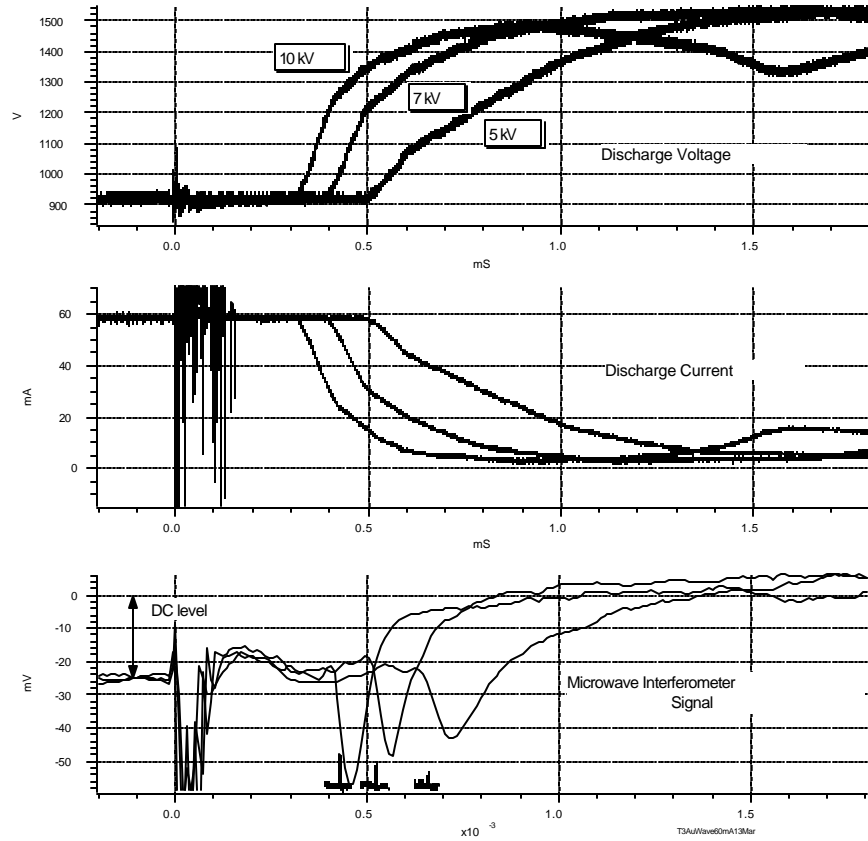


Figure 17. Discharge Voltage (Top), Current (Center), and Microwave-Interferometer Signal (Bottom) for a 3-Torr, 60-mA Discharge in N_2 . Laser-photo-deflection signals in the bottom diagram indicate the time of the shock wave passing through the interferometer focal volume. Large spikes at $t=0$ are caused by the spark discharge-shock generator.

recombination coefficient $k_r=2 \times 10^{-6}$ (for N_4^+ , since the pressures is above ~ 1 Torr) and pressure of 6 Torr, corresponding to a density increase of a factor of two behind the shock wave, the decay was computed for two cases: 1) electron temperature $T_e=1$ eV, initial electron density $n_e=3 \times 10^9 \text{ cm}^{-3}$ and 2) $T_e=2$ eV, $n_e=10^{10} \text{ cm}^{-3}$. While the electron density for the first case approximates the actual electron density in our discharge, T_e is high since we can assume that T_e rapidly decays to about the long-lived vibrational temperature of ~ 0.3 eV. The computed decays are compared with the measured decays in a logarithmic plot in Fig. 18. The first case represents the slower computed decay in Fig. 18--slower than any of the current or density decays. Also note that its curvature indicates that recombination is a major contributor to the losses. To simulate a larger loss by diffusion, in the second case the electron temperature and the initial electron density were increased. Even with these high values, the computed decay is

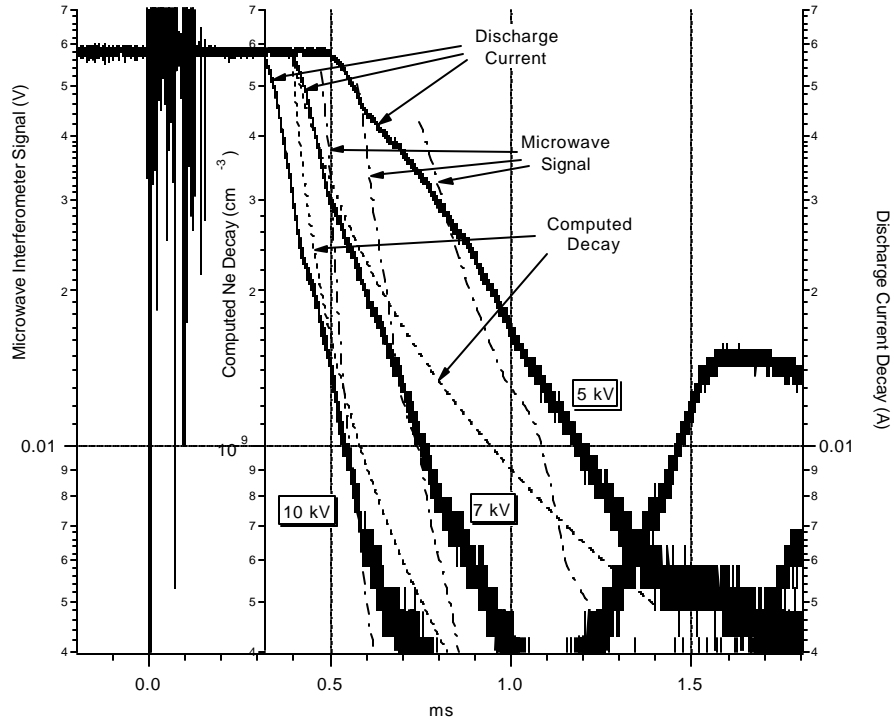


Figure 18. Logarithmic Display of the Global Discharge Current and the Local Electron-Density Decay for Three Shock Strengths. Data are the same as in Fig. 17. Computed electron-density decays are for a pressure of 6 Torr, a recombination coefficient $k_r=2 \times 10^{-6}$, and the following two parameter sets: a) (slower decay) $N_e=3 \times 10^9 \text{ cm}^{-3}$, $T_e=1 \text{ eV}$ and b) (faster decay) $N_e=10^{10} \text{ cm}^{-3}$, $T_e=2 \text{ eV}$.

barely as fast as the electron-density decay for the slowest shock wave and still exhibits losses by recombination. The higher loss rate shown in the experimental results could be caused by loss to the discharge electrodes. While the E/n decreases behind the shock front as a result of the density increase, it still remains at least 50% of the original value (assuming a density increase of a factor of two) and continues to increase. Thus, even with a reduced drift velocity, charge-carrier losses to the electrodes continue but ionization by electron impact does not.

He-Metastable Density in a Double Layer

The population-density profile of triplet metastable He in the region of a double layer formed at an abrupt transition in the diameter of a gas discharge was measured by laser-diode absorption and spatially resolved plasma-induced emission. The double layer thus formed is the transition region between areas of plasma with different characteristics, such as electron temperature and electron density, which are functions of the discharge-tube diameter.¹¹⁻¹³ The change in triplet

metastable-He population density in the double-layer region when the cathode end of the discharge was in the large-diameter tube was measured and compared to that when the anode end of the discharge was in the large-diameter tube. The reduced electric field, E/n could be determined from these profiles in the region of the double layer since the change in triplet metastable-He density follows the change in the local electric field and electron density.¹⁴

A diagram of the experimental arrangement is shown in Fig. 19. The Pyrex discharge cell was constructed with two concentric tubes of different diameters. To form the double layer, the inner smaller diameter tube (8-mm o.d., 6-mm i.d., 10-cm length) is sealed inside the larger (30-mm o.d., 26-mm i.d., 40-cm length) discharge cell such that the discharge is only continuous through the smaller diameter tube. The 2.5-cm cup electrodes are equi-distant from the inner tube in side arms of the main discharge cell. The diode-laser output enters and exits the discharge cell through two opposed windows (2.5-cm diameter), positioned such that the window centers are ~ 3 mm from the end of the inner tube. The discharge cell was baked out under high vacuum,

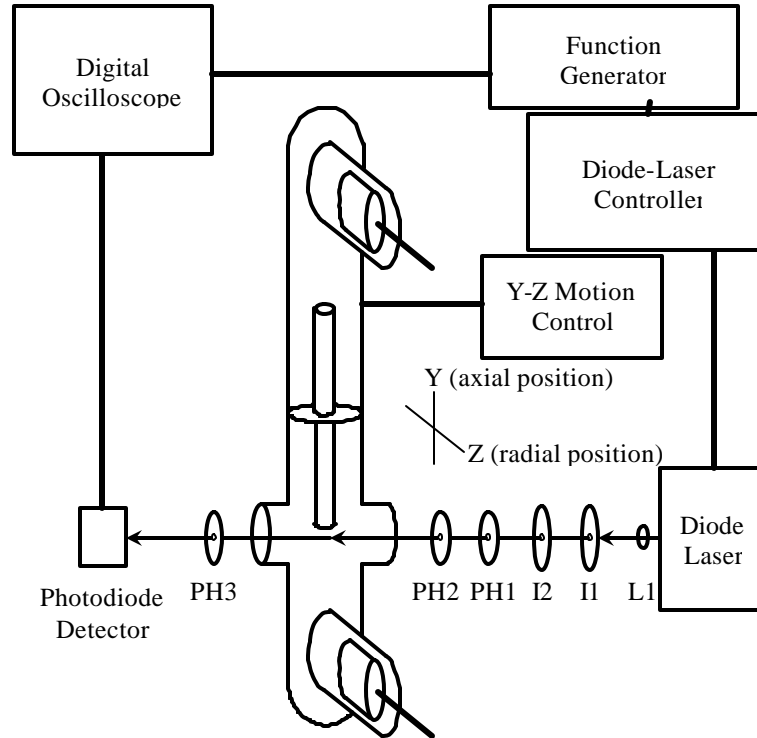


Figure 19. Schematic Diagram of the Experimental Apparatus. L1 is an aspherical lens; I1 and I2 are iris diaphragms; PH1 is a 200- μ m pinhole; and PH2 and PH3 are 500- μ m pinholes.

filled with ultra-high-purity He (99.999%) to 1-Torr pressure, and then sealed. The discharge voltage was applied from a constant-voltage power supply in series with a 50-k Ω ballast resistor. Absorption and emission measurements were performed for fixed discharge currents of 1, 2, and 5 mA.

The diode-laser absorption-spectroscopy technique has been described by Millard *et al.*¹⁵ In brief, the diode-laser wavelength was scanned through the metastable He $2^3S_1 \rightarrow 2^3P_J$ transitions by external voltage control of the diode current. The metastable 2^3S_1 He spatial profiles were obtained by scanning the discharge cell relative to the laser. The discharge cell was mounted on a motorized Y-Z translation stage that could be step scanned in 1 μm increments. For axial profiles the radial Z position was held fixed while the translation stage was step-scanned in the Y-direction. Radial profiles were obtained by scanning the Z position at fixed Y positions. An InGaAs photodiode detector monitored the transmitted diode-laser signal. The diode-laser spatial resolution was defined by collimating the laser output with an aspherical lens (L1) before passing the collimated beam through the series of iris diaphragms and pinholes (I1 through PH2 in Fig. 19). The spatial resolution was roughly 200 μm (determined by PH1).

Three diode-laser transmission signals were recorded at each axial cell position: the metastable-He absorption signal (I_t), a reference absorption signal with the discharge off, (I_0), and a background signal (I_b) with the discharge on and the laser blocked. The metastable-He absorption signal was then $(I_t - I_b)/I_0$. A typical metastable-He transmission spectrum is given in Fig. 20.

The absorption spectrum was fit using Beer's law. The transmitted signal is given by

$$I_t = I_0 \cdot \exp(-\sigma \cdot N \cdot l) \quad (4)$$

where σ is the absorption cross section, N the metastable-He number density, and l the absorption path length through the discharge. The absorption cross section can be determined from the spontaneous-emission rate, A_{21} , and is given by

$$\sigma = A_{21} \cdot (\lambda^2/8 \pi n^2) \cdot g_2/g_1 \cdot g(v) \quad (5)$$

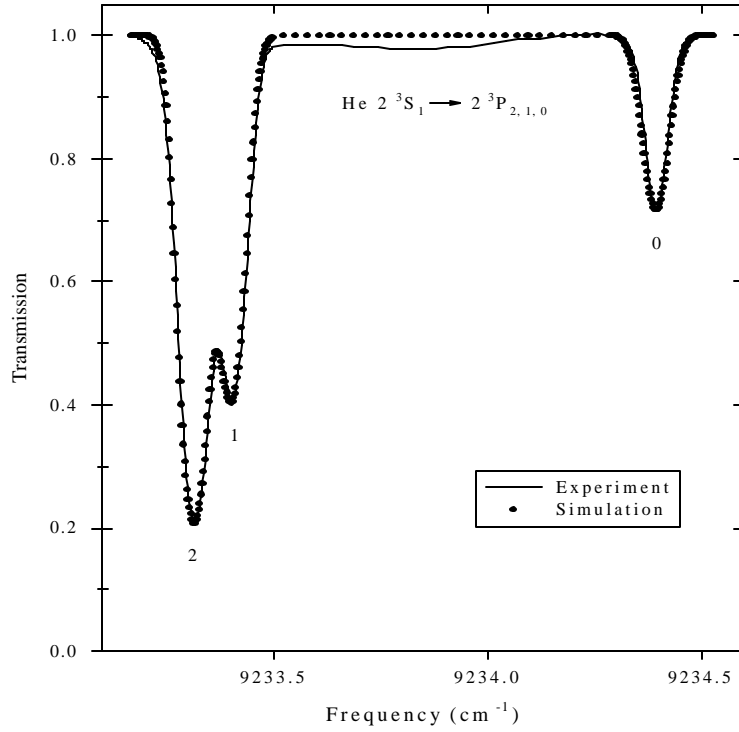


Figure 20. Experimental Absorption Spectrum and Simulation of Metastable-He $2^3S_1 \rightarrow 2^3P_{0,1,2}$ Transitions in 1-Torr He at 2-mA Discharge Current. Solid line is the experimental spectrum, and the dotted curve is the simulation.

where $A_{21} = 1.022 \times 10^7 \text{ s}^{-1}$ (from Ref. 16), λ the transition wavelength, g_2 and g_1 the upper- and lower-state degeneracies, respectively, and $g(v)$ an area-normalized Doppler lineshape function. Since the spatial-number-density distribution $N(x,y,z)$ is not uniform in the discharge, the line-integrated metastable-He density, $N \cdot l$, is determined. Along with the line-integrated density, a Doppler width can be determined from a simultaneous fit of the three transitions in Fig. 20.

The axial profile was measured by stepping the discharge cell, with the motorized translation stage, relative to the laser position. The cell vertical (Z direction) was held fixed at the center of the smaller, inner tube as the cell was stepped in the horizontal (Y direction), perpendicular to the laser axis (X direction). The metastable-He density was measured inside the smaller diameter tube, through the diameter transition, and in the larger diameter tube, i.e., on both sides of the abrupt diameter transition. Axial profiles of metastable-He line-integrated density at 1, 2, and 5 mA at the cathode end and anode end of the discharge are shown in Figure 21. From the

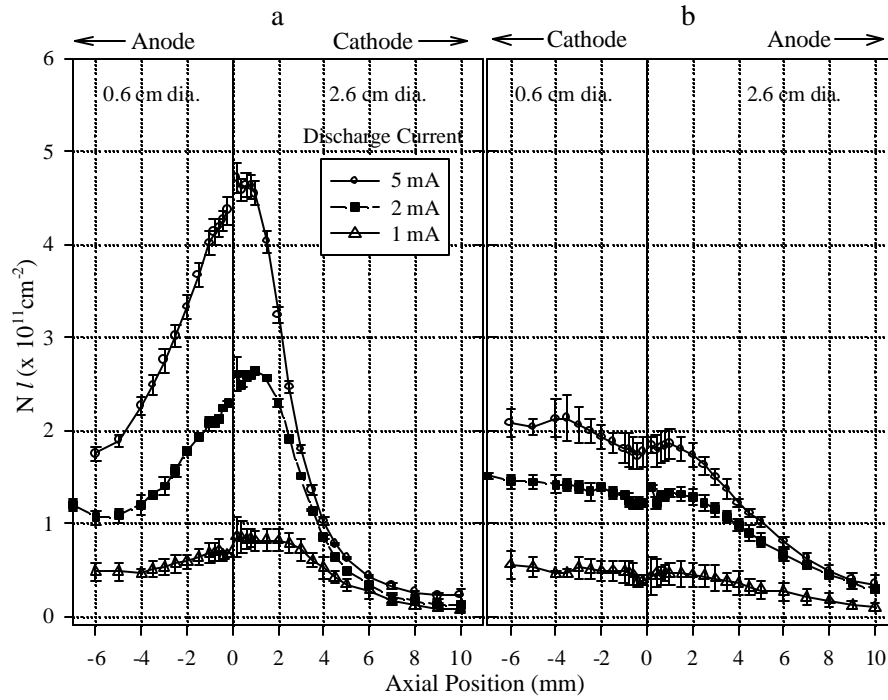


Figure 21. Axial Profiles of the Line-Integrated Density of He 3S_1 for 1-, 2-, and 5-mA Discharge Currents. Position of the tube-diameter transition is 0 mm. Tube diameters are indicated in the figure.

figure, it can be seen that the metastable-He density profiles are polarity dependent. For the case of the anode in the large-diameter-tubing end of the discharge, the 3S_1 He density is roughly constant in the smaller diameter tube and then decreases monotonically in the larger diameter tube. For the case where the cathode is in the large-diameter-tubing end, the 3S_1 He density has a pronounced maximum in the transition region. The 3S_1 He metastable density is enhanced by a factor of four for the 5-mA discharge relative to the metastable-He density at the anode end. The magnitude of the enhancement increases with increasing current, while the position of the peak in the enhancement decreases with current, i.e., the 3S_1 He density is enhanced to a greater extent nearer the transition for the higher current discharge.

The 3^3D He metastable density profile was obtained in much the same way as the 3S_1 He density by measuring the plasma emission with a photomultiplier tube (PMT) through a 588-nm bandpass filter. The photodiode detector in Fig. 19 was replaced with a 1P28 PMT and the plasma emission viewed through the 500- μm pinhole (PH3), which determined the spatial resolution of the emission profiles. As in the diode-laser absorption experiments, the discharge

cell was scanned relative to the pinhole/PMT. The axial profiles of the $^3\text{D He}$ for 1, 2, and 5 mA are shown in Fig. 22. The $^3\text{D He}$ metastable axial profiles exhibit the same behavior as the $^3\text{S}_1$ density profiles. The emission profiles are polarity dependent, with the cathode profile showing an enhancement relative to the anode profile. The maximum in the enhancement is also ~ 1 mm from the end of the inner tube.

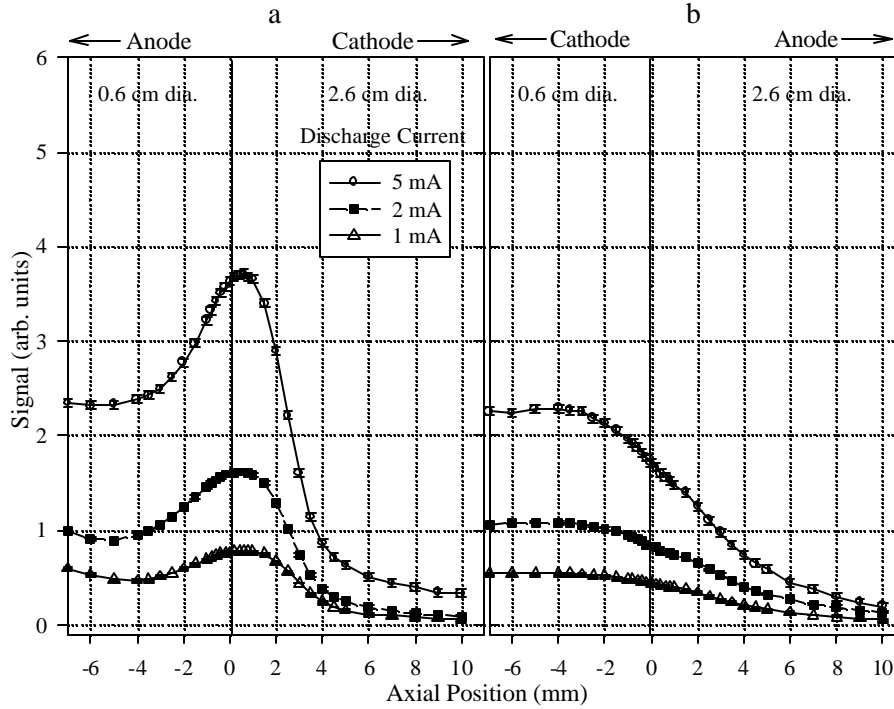


Figure 22. Axial Emission Profiles of $^3\text{D He}$ Metastable for 1-, 2-, and 5-mA Discharge Currents. Position of the tube-diameter transition is 0 mm. Tube diameters are indicated in the figure.

The axial profiles for both the $^3\text{S}_1$ and $^3\text{D He}$ metastables exhibit polarity-dependent enhancement of the metastable densities in the region of the double layer formed at the diameter transition. The metastable-He population-density enhancement increases with discharge current and is evident in the case of the cathode in the larger diameter tube section. There is less metastable He is present, and the radial profiles are not so peaked when the anode is in the wider tube section. From a simple analysis of the metastable-He density measurements, the axial profile of the reduced electric field, E/n , can be estimated, assuming that the electron-energy-distribution function (eedf) is in equilibrium with the reduced electric field. The triplet metastable He density can be calculated from a balance equation for the production and loss of

metastable He 2^3S_1 atoms.^{17,18} The triplet metastable He balance equation at steady state is given by:

$$D\nabla^2 N_{\text{He}^*} + k_{\text{exc}} n_e N_{\text{He}} - k_{\text{ion}} n_e N_{\text{He}^*} - k_{\text{He}^*} N_{\text{He}^*}^2 = 0 \quad (6)$$

where $D\nabla^2 N_{\text{He}^*}$ is the triplet metastable-He diffusion loss to the wall ($= -D(2.405/r)^2 N_{\text{He}^*}$, assuming the fundamental diffusion mode). N_{He} and N_{He^*} are the densities of ground- and triplet- metastable-state He, respectively, while n_e is the electron density. k_{exc} is the rate coefficient for the production of triplet metastable He; k_{ion} is the rate coefficient for ionization loss of triplet metastable He; and k_{He^*} is the rate coefficient for the loss of triplet metastable He by triplet-triplet metastable collisions. The triplet metastable-He diffusion coefficient was taken from Phelps¹⁹, while the production and loss-rate coefficients of Miller, Verdeyen, and Cherrington¹⁷ were used.

The reduced electric field can be determined from the scaling relationships of low-pressure He discharges²⁰ in the small- and large-diameter discharge tubes, well away from the tube-diameter transition. The electron density inside the small diameter tube was calculated, assuming current continuity, from the electron drift velocity in a He gas discharge²¹ and the reduced electric field determined from the scaling relationships.²⁰ To simplify the calculation of the reduced electric field from the measured line-integrated metastable-He density, a constant electron density and a constant optical path were assumed for all points inside the smaller diameter tube and for 4 mm past the tube-diameter transition in the wider diameter tube. The excitation (k_{exc}) and ionization (k_{ion}) rate coefficients in Eq. (6) are functions of the reduced electric field¹⁷, while the metastable-He loss-rate coefficient (k_{He^*}) is constant.^{17,19} The rate-coefficient data set of Miller, Verdeyen, and Cherrington¹⁷ was extrapolated to higher values of reduced electric field by fitting their values to an exponential growth for k_{exc} and an exponential rise to a maximum value for k_{ion} . The data and extrapolation are shown in Fig. 23. To compare the measured line-integrated metastable-He density with the metastable-He number density calculated from Eq. (6), the calculated number density was transformed to a line-integrated density by multiplication with a derived optical path. The reduced-electric-field profiles were determined by fitting the measured metastable-He densities with Eq. (6) by varying the values of the rate coefficients k_{exc} and k_{ion} (which are functions of the reduced electric field).

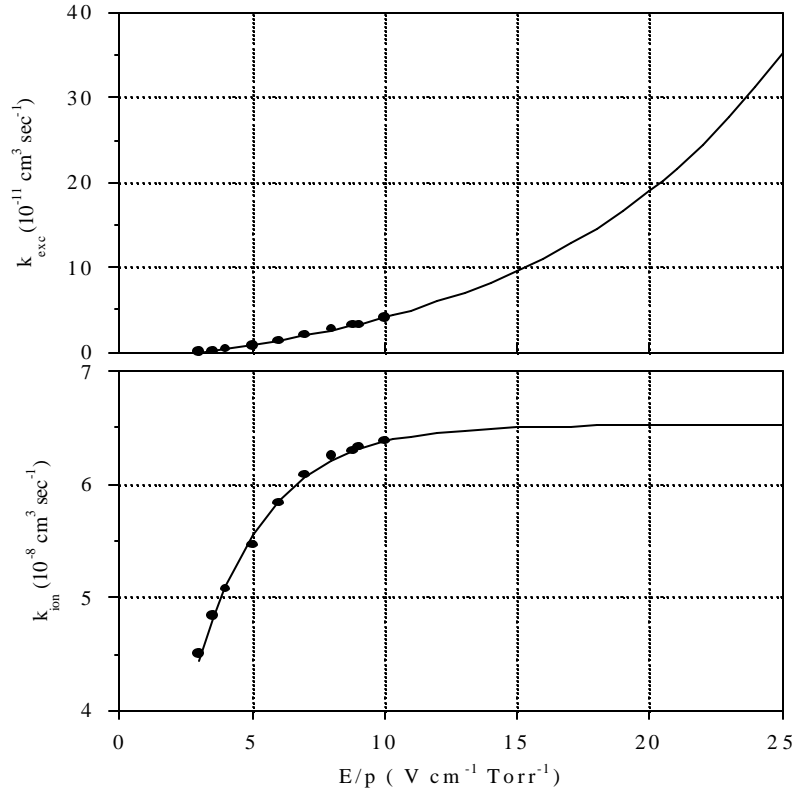


Figure 23. Triplet-Metastable-He Excitation and Ionization Rates. Data points are taken from Ref. 17, and the solid lines are extrapolations.

The reduced-electric-field axial profiles derived from the metastable-He density profiles are shown in Fig. 24. The axial profiles for the cathode in the larger diameter tube are shown in Fig. 24a; those for the anode in the wide tube section are shown in Fig. 24b. The axial E/n profile goes through a maximum in the region of the double layer at the diameter transition when the cathode is in the wider tube section. A simple, self-consistent explanation for the difference with discharge polarity of the axial profile of the reduced electric field near the diameter transition could be that the electric fields are additive in one case and subtractive in the other while satisfying current continuity requirements imposed by the diameter discontinuity of the positive column. The local increase in the electric field would then be greater when the cathode is in the larger diameter tube than when the anode is in the wide section.

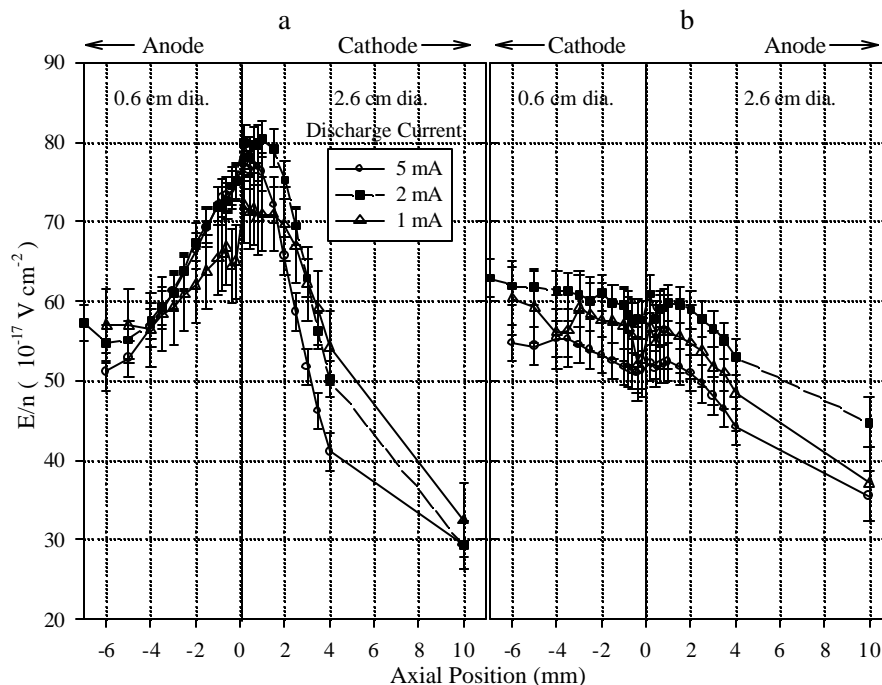


Figure 24. Reduced-Electric-Field Axial Profiles in the Region of the Double Layer for 1-, 2-, and 5-mA Discharge Currents. a) Reduced Electric Field with the Cathode in the Larger Diameter Tube. b) Reduced Electric Field with the Anode in the Wider Tube Section. The tube-diameter transition is at 0 mm, and the negative axial positions are inside the smaller diameter tube.

H-Atom Measurement in a $\text{H}_2\text{-N}_2$ Pulsed Glow Discharge

The concentration of H-atoms in a gas discharge can be conveniently measured by two-photon-absorption laser-induced fluorescence (TALIF). Bletzinger and Ganguly used TALIF to determine the concentration of H-atoms in a $\text{H}_2\text{-N}_2$ mixture for an inductively coupled helical-resonator discharge, a parallel-plate rf discharge, and a microwave discharge.²² Their results indicated that the H_2 dissociation in the $\text{H}_2\text{-N}_2$ gas mixture must involve interactions of vibrationally and electronically excited N_2 molecules with the H_2 .

A fixed-separation, parallel-plate gas-discharge cell was constructed to examine the effect of pulse duration on H-atom production. The main components of the apparatus were the discharge cell, the electronics, and the probe laser system. The discharge cell was a cylindrical glass cell, roughly 37 cm in height and 7.5 cm in diameter. Two sets of opposed windows (5-cm diameter),

orthogonal to each other, were located roughly 25 cm from the bottom of the cell; one set of windows permits passage of the laser through the cell, and the other allows viewing of the laser-excited fluorescence or plasma emission. The laser entrance and exit windows were made of high-quality fused silica, and the fluorescence-viewing windows were made of BK-7. The cell was evacuated through 3.5-cm-i.d. glass and metal lines by an Alcatel 5010 drag pump, backed with an oil-free diaphragm pump. With no gas flowing, the system pumped down to < 1 mTorr.

The discharge gas flows were controlled with flow controllers (MKS Type 1259 flow controller) and an MKS Type 247C four-channel readout, while the cell pressure was maintained by a control valve and an exhaust-valve controller (MKS Type 253A and 252, respectively). The cell pressure was measured with a baratron pressure gauge (MKS Type 102A) whose output was sent to the valve controller for maintaining a constant pressure in the discharge cell. The gas flow could be varied from 0 to 100 SCCM, and the baratron pressure gauge operated in the range 0-10 Torr. The gases were externally mixed, after the flow controllers, and entered at the top of the cell through an internal glass-tubing loop with evenly spaced 1-mm holes. Both the H_2 and the N_2 discharge gases were obtained from Matheson (UHP grade, 99.999%).

The discharge electrodes were two aluminum discs, 5 cm in diameter with an inter-electrode spacing of 7 cm. The discharge voltage was provided by a current-regulated, pulsed power supply. The current was adjustable to 1.5 A, and the voltage was adjustable to 12 kV. The pulse width could be adjusted from 5 μ s to 1.1 ms, with pulse rise and fall times of < 0.5 μ s (with a 5-k Ω ballast resistor) and a repetition rate of single shot to 20 Hz.

The H-atom TALIF measurements were performed with a cell pressure of 2.5 Torr, a total gas flow rate of 40 SCCM, and a constant discharge current of 250 mA. The cell pressure, gas flow rate, and gas mixture were computer controlled. The duration of the discharge pulse was varied from 10 μ s to 1 ms and synchronized with the laser probe pulse by a Stanford Research DG535 delay generator, which was also computer controlled. The hydrogen atoms were probed 20 μ s after the discharge pulse was turned off.

The discharge voltage and current were measured with a high-voltage probe and a current probe for various cell pressures, electrode spacing, and hydrogen–nitrogen gas mixtures. The cell pressure was varied from 1 to 4 Torr and the electrode spacing from 4.6 to 9.7 cm, while the percentage of hydrogen in the gas mixture was 100, 80, 50, and 20. The discharge voltage, at constant current, varied with cell pressure, electrode spacing, and gas mixture. This variation was minimized for a cell pressure of 2.5 Torr and electrode spacing of 7.1 cm. It is necessary to reduce the discharge-power variation as a function of gas mixture to achieve better isolation of the contribution to hydrogen-atom production from heavy-particle collisions in the gas mixtures. The variation of the discharge voltage with H_2 fraction for discharge-pulse durations of 10 μs - 1.0 ms was measured with a high voltage probe and is shown in Fig. 25. The discharge voltage varies only slightly ($< 10\%$) with H_2 fraction in the gas mixture over the entire range of H_2 fraction in the gas mixture.

The discharge electric field was also determined for the different discharge pulse durations and gas mixtures used for the H-atom concentration measurements. The discharge cell was modified

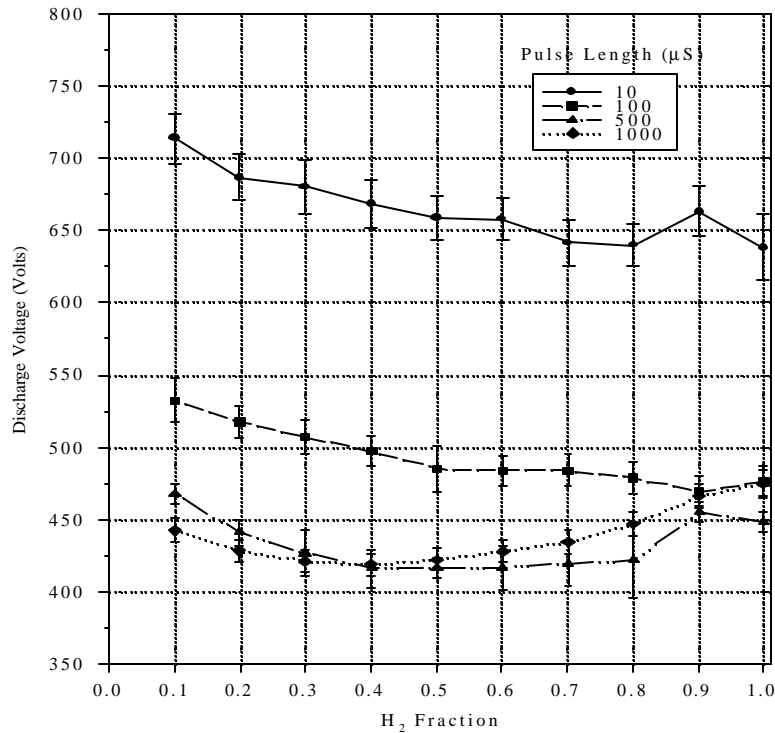


Figure 25. H_2 - N_2 Discharge Voltage as a Function of Gas Mixture and Pulse Duration. H_2 is the fractional flow of H_2 in the H_2 - N_2 gas mixture.

by replacing the fixed-anode electrode with a movable electrode of the same diameter and made from the same material. The electrode-gap spacing was then incrementally changed around the 7.1-cm gap used in the H-atom TALIF experiments, and the discharge voltage was measured with a high-voltage probe. Plots of discharge voltage as a function of gap spacing were linear, and the slopes of these curves, with 7.1 cm being the center point, determined the electric field. The determined electric fields are shown in Fig. 26. The 10-, 100-, and 1000- μ s pulses monotonically increase with N_2 dilution, and the shapes agree with the calculation of Garscadden and Nagpal.²³ However, the electric fields for the 200- and 500- μ s pulses decrease with the addition of N_2 but then monotonically increase with the addition of N_2 . This effect is not predicted in the calculation.

The relative H-atom signals were measured as a function of H_2 fraction in an H_2 - N_2 gas mixture at a constant pressure and discharge current. Since it is known that H-atom fluorescence is quenched more by N_2 than by H_2 , it was necessary to examine the temporal decay of the H-atom

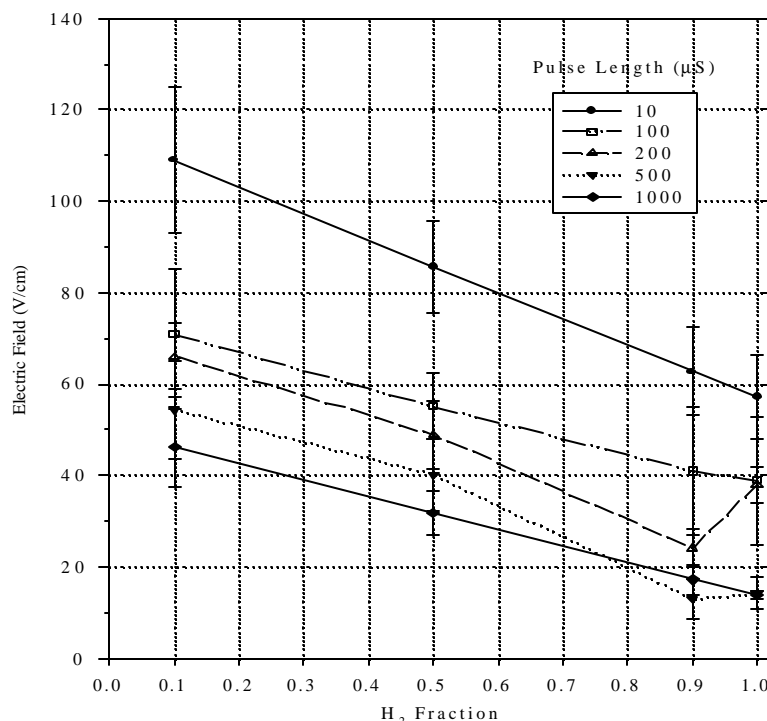


Figure 26. Determined Electric Field for the H_2 - N_2 Gas-Mixture Discharge. The gas pressure was 2.5 Torr, and the current was 250 mA. The pulse length is the duration of the discharge.

fluorescence for different mixtures of H_2 in N_2 . Figure 27 shows the photomultiplier fluorescence waveform for various gas mixtures of H_2 - N_2 , along with a scattered-light waveform of the 6-ns probe laser. As can be seen in the figure, the H-atom fluorescence signal is just slightly longer than the scattered-light signal, but no measurable difference is observed under these experimental conditions among the lifetimes of the fluorescence decays for the gas mixtures here. Thus, either the system response time is not sufficiently rapid to resolve temporal changes in the decay or the dominant quencher of the H-atom fluorescence is neither H_2 nor N_2 . Since no difference was observed experimentally, no correction was applied.

The H-atoms were measured 20 μs after the discharge pulse since this time was sufficiently long after the pulse that no plasma-emission background signal remained but sufficiently short that

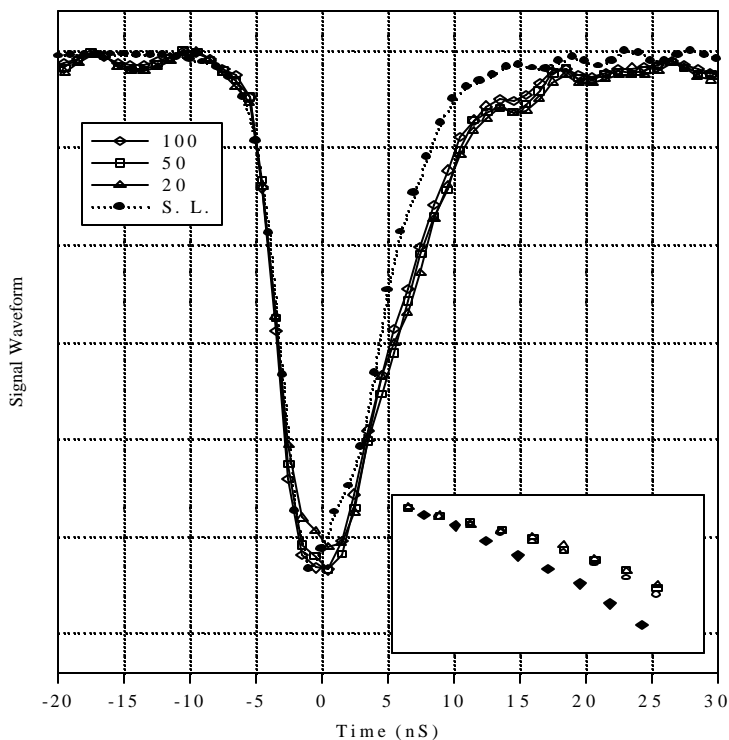


Figure 27. H-Atom-Fluorescence Waveform for Various H_2 - N_2 Gas Mixtures. Waveform peak heights were adjusted to the same scale (100, 50, and 20% H_2). The waveform with closed circles (S.L.) was recorded with the discharge off and the probe-laser scattering from a pin at the focal point of the PMT collection optics. The inset is a semi-log plot of the decay portion of the waveform. Except for the scattered-light line, the slopes of the lines for the different gas mixtures are the same within experimental uncertainty.

the H-atoms produced by the discharge could not diffuse from the viewing region. This was verified by observing the temporal decay of the H-atom signal after the discharge was turned off. The signal was constant for roughly 200 μs after the discharge pulse and then decayed for longer times, as displayed in Figs. 28 and 29. Figure 28 shows the temporal decay of the H-atom signal 200 μs after the pulse for different $\text{H}_2 - \text{N}_2$ gas mixtures, while Fig. 29 shows the decay up to 5 ms after the pulse for a pure H_2 discharge. Figure 29 also shows the relative H-atom signals in a pure H_2 discharge for 200-, 500-, and 1000- μs duration discharge pulses. It can be observed that the H-atom signal from the discharge pulses of various duration (closed diamonds) lies on the temporal-decay curve of the fixed-pulse-length signal (open circles). Thus, the fact that longer pulse length signals are lower than the 200- μs pulse can be attributed to diffusion.

The background plasma emission during the discharge pulse, viewed by the PMT through a 656-nm bandpass filter (corresponding to H_α emission), was also recorded for the different discharge-

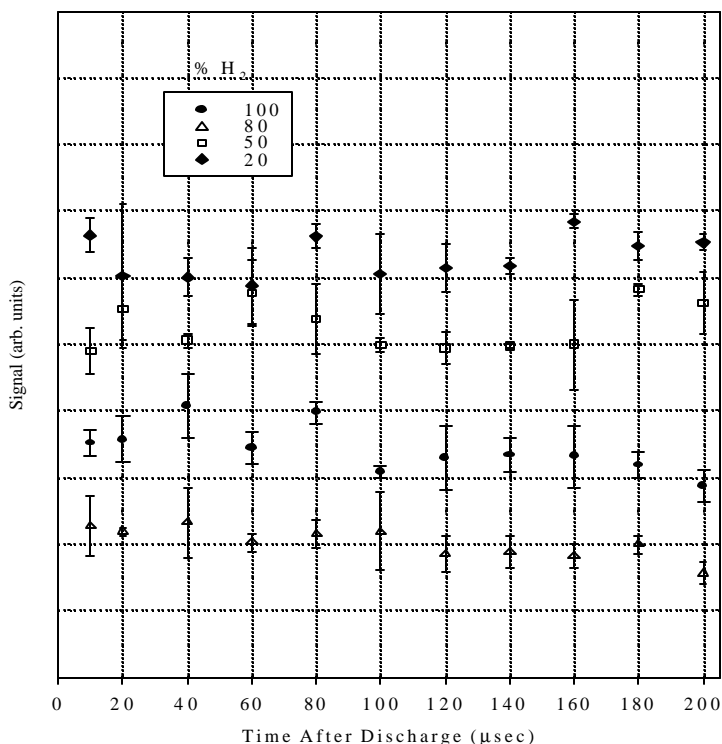


Figure 28. Temporal Decay of H-Atom TALIF Signal for Different $\text{H}_2 - \text{N}_2$ Gas Mixtures for a Cell Pressure of 2.5 Torr and a 500- μs , 250- mA Discharge Pulse. The delay time is the time at which the H-atoms were measured after the discharge pulse was turned off.

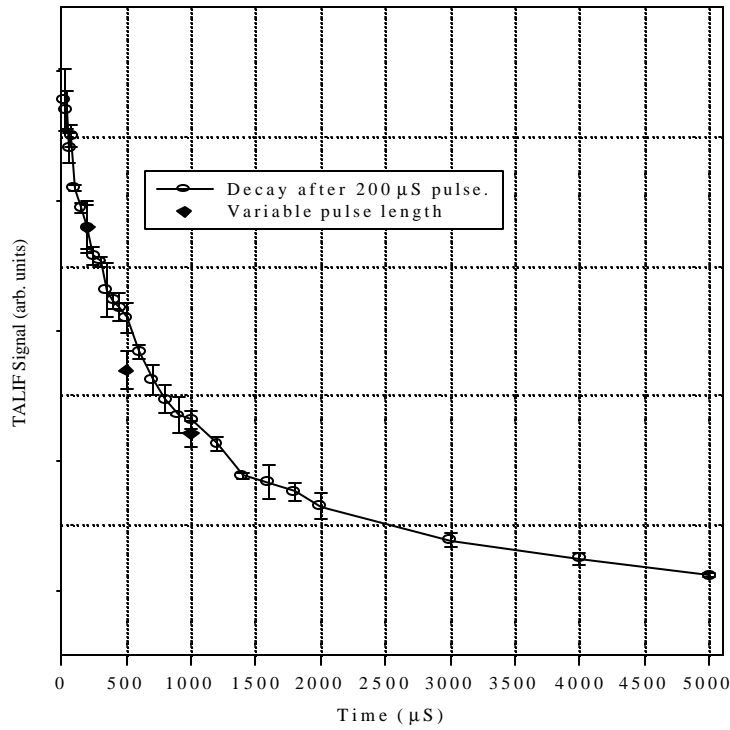


Figure 29. Temporal Decay of the H-Atom TALIF Signal for a 100% H_2 , 2.5-Torr, 250-mA Discharge. The open circles represent the signal decay after the discharge pulse is turned off for a 200- μs pulse. The closed diamonds correspond to the relative signal levels of the H-atom, probed 20 μs after the discharge pulse is turned off for pulses of 200, 500, and 1000 μs .

pulse durations. The background plasma emission for 100- and 1000- μs discharge pulses in a pure H_2 discharge is shown in Fig. 30. The emission for the 1000- μs pulse (solid curve) shows an initial burst of H_α emission in the first 200 μs , followed by a constant level for the remainder of the discharge pulse. The 100- μs pulse (dotted curve) has the same shape as the first 100 μs of the longer 1000- μs pulse before shutting off at 100 μs . The H_α emission for all of the pulse durations used is of the same temporal shape and can be visualized by truncating the 1000- μs pulse at the appropriate time. From the determined electric field, E/n values can be estimated. The plasma emission decreases with pulse duration up to 200 μs , as does the electric field. Thus, for the shorter discharge pulses, it is assumed that gas heating is negligible and that the number density does not change. At longer times the electric field decreases, but the plasma emission is constant, which implies that E/n is constant because of a lower number density that results from gas heating.

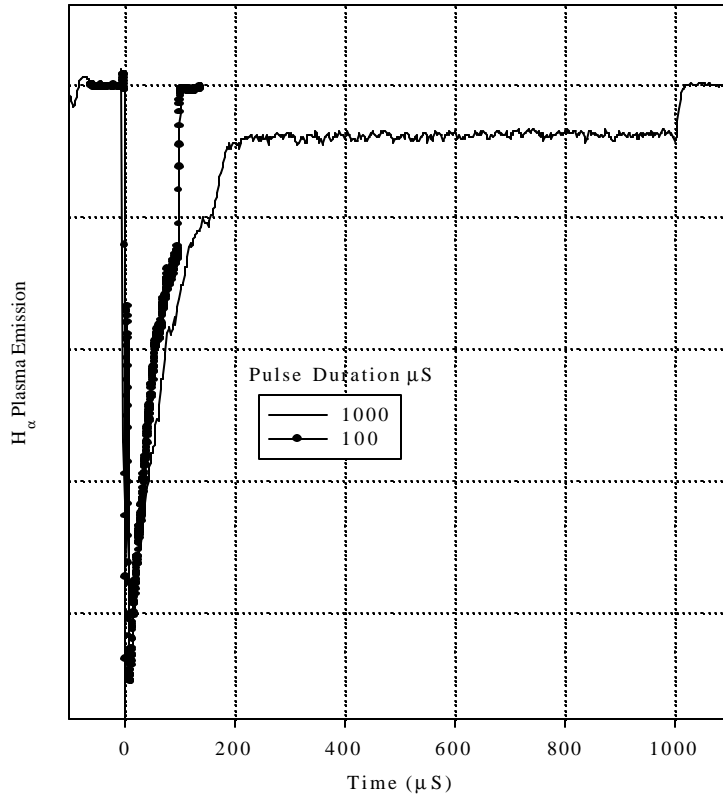


Figure 30. H_{α} Plasma Emission in a H_2 Discharge for 100- and 1000- μs Discharge Pulses.

Hydrogen dissociation in the mixed-gas discharge was measured with discharge pulse durations of 10, 100, 200 and 1000 μs (at constant current). The relative H-atom TALIF signal as a function of H_2 fraction in the H_2 - N_2 gas mixture is shown in Fig. 31. Although the relative signal level is lower for the 10- μs -duration discharge pulse than for the 100- μs pulse (note that the signal has been magnified 5X in Fig. 31), the two curves are essentially the same; the relative H-atom signals decrease monotonically with increasing N_2 fraction in the gas mix. The shapes of the relative signal curves for the longer duration discharge pulses are not the same as those for the short pulses (10 and 100 μs). The H-atom signal initially decreases with the addition of N_2 and then increases with further addition until it levels off for 10-60% H_2 in the gas mix for the 1000- μs -duration pulse. For the 200- μs pulse, the signal initially decreases and then increases with the addition of N_2 , as in the case of the 1000- μs pulse, but the signal decreases again after reaching a maximum at 60-70% H_2 . The nearly constant H-atom signal for the 1000- μs pulse

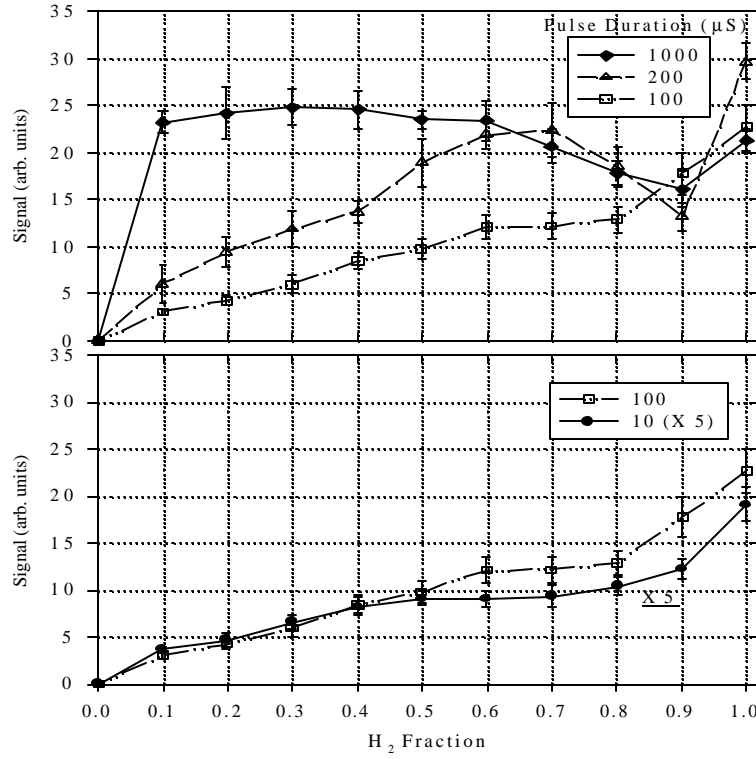


Figure 31. Relative H-Atom TALIF Signal as a Function of the Discharge Pulse Duration. Discharge conditions are the same as in Fig. 25. Note that the signal for the 10-μs discharge pulse (bottom graph) has been multiplied by 5X to facilitate comparison with the 100-μs pulse signal.

with 10-60% H₂ indicates that the fractional dissociation of H₂ is increasing with N₂ concentration for the longer pulse.

The relative H-atom TALIF signals for the different discharge pulse durations were calibrated to an absolute scale with the calculated fractional-power deposition in H dissociation²⁴ and the determined E/n values. The fractional powers deposited into different inelastic modes (electronic, vibration, rotation, and dissociation) in pure H₂ and N₂ discharges as a function of E/n are given in Ref. 24. From the discharge conditions the total power was determined for each pulse duration; with the calculated fractional-power deposition into H₂ dissociation, the energy density for each pulse was estimated for a pure H₂ discharge. The H-atom densities for the pure-H₂ discharges were calculated, assuming an energy dissipation of 10 eV in H₂ dissociation. The results are summarized in Table 2. It was assumed that gas heating for the longer discharge pulses decreases the volume electric field and that the E/n values are constant for discharge

Table 2

Volume Electric Field, E/n Values, Power, and H-Atom Density Obtained
from Calculated Fractional Power Dissipated in H₂ Dissociation.

t (μs)	E (V/cm)	E/n (Td)	P (W/cm ³)	% P ²⁴	E _H x10 ⁻⁶ (J/cm ³)	[H] x10 ¹³ (cm ⁻³)
10	57±9	70±11	0.73±0.11	54±4	4.0±0.7	0.50±0.08
100	39±14	48±17	0.50±0.18	38±12	19.0±0.9	2.4±1.2
200	38±14	47±5	0.48±0.05	38±12	36.5±1.2	4.4±1.4
500	14±3	47±8	0.18±0.04	38±12	34.2±1.3	4.2±1.6
1000	14±3	47±3	0.18±0.01	38±12	68.4±2.2	8.4±2.8

pulses longer than 200 μs (gas heating lowers the number density at constant pressure) [see the previous discussion of the observed H_α plasma emission (Fig. 30)].

The relative H-atom TALIF signal was then calibrated to the calculated H-atom densities (derived from the E/n values and fractional-power-deposition calculations) by normalizing the H-atom TALIF signal for a 10-μs discharge pulse in a pure H₂ discharge. Negligible gas heating should occur with a 10-μs discharge pulse; thus, the number density will not be affected by any temperature rise in the constant-pressure discharge. The H-atom TALIF signals for the other discharge pulse durations were then scaled from the 10-μs point. The 500- and 1000-μs TALIF signal levels were corrected for the previously measured temporal decay of the signal before being scaled to the absolute number density. The H-atom densities from the fractional-power calculation and scaled TALIF signals are shown in Fig. 32 and are in excellent agreement. The relative H-atom TALIF signal for the various discharge pulses as a function of gas mixture was then calibrated to absolute number density from the 100% H₂ TALIF signals of Fig. 32. The calibrated H-atom density as a function of discharge pulse length and H₂ fraction is shown in Fig. 33.

The enhancement of fractional H₂ dissociation with pulse duration is evident in Fig. 34, where the H-atom density (as a percentage of H₂ in the H₂-N₂ gas mixture) is shown as a function of pulse duration and gas mixture. For discharge pulses up to 200 μs, the increase with pulse

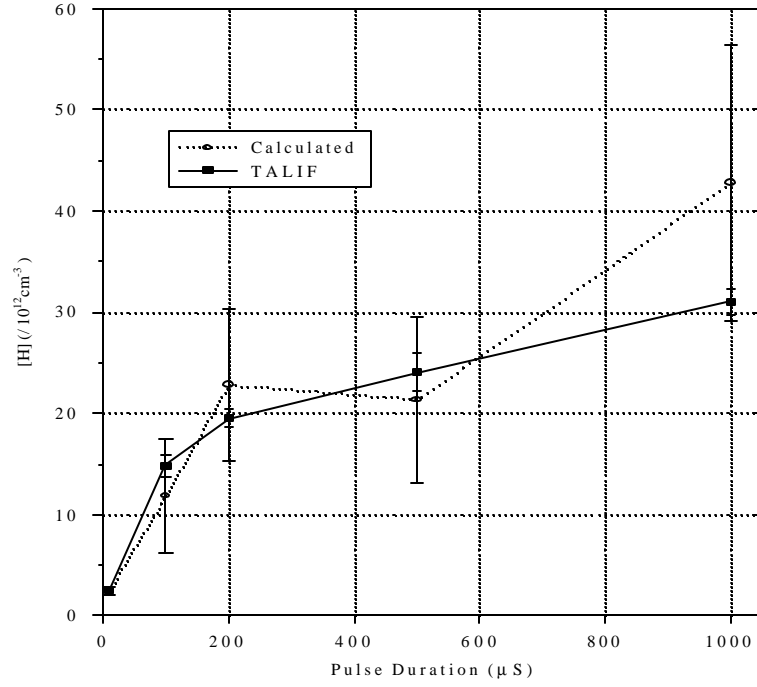


Figure 32. H-atom TALIF Signal Calibration for a H_2 Discharge from a Power-Deposition Calculation. The relative TALIF signal and calculated H-atom density were normalized at $10 \mu\text{s}$.

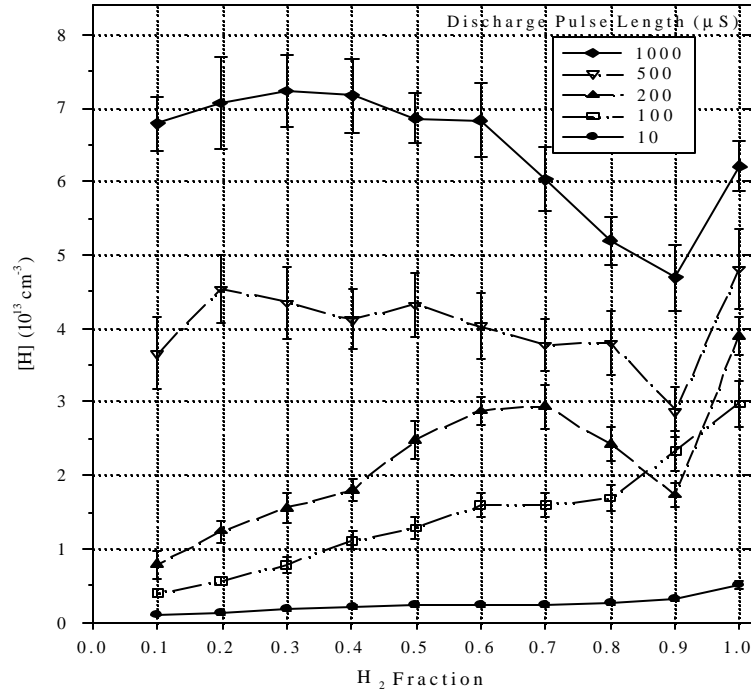


Figure 33. Absolute H-atom Density as a Function of Discharge Pulse Length in a $\text{H}_2\text{-N}_2$ Pulsed Discharge.

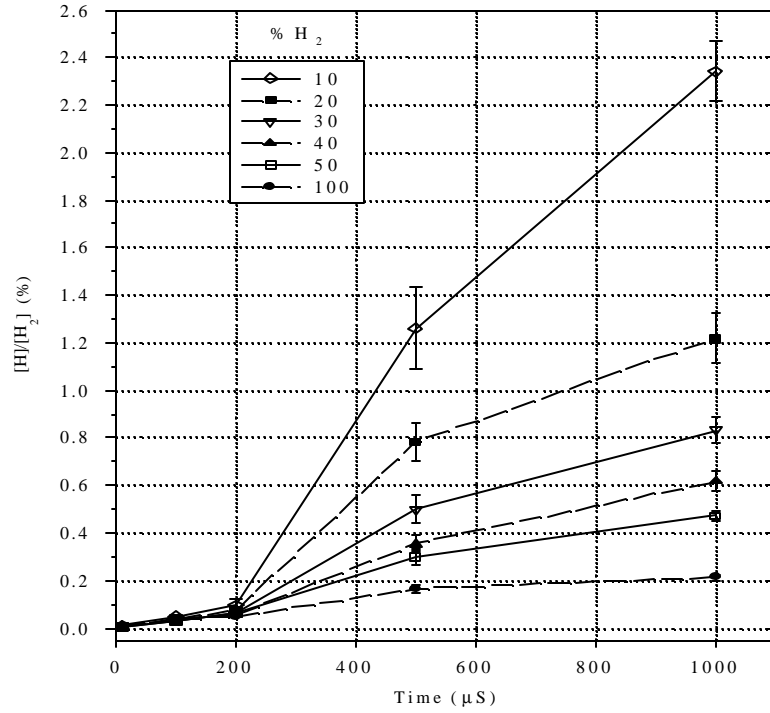


Figure 34. Fractional H₂ Dissociation as a Function of Discharge-Pulse Duration for Different Gas Mixtures in a H₂–N₂ Discharge.

duration is small, and no dependence on N₂ concentration is observed; while for longer pulses where heavy-particle collisions become significant, the increase in the fractional dissociation of H₂ with N₂ dilution is large.

The absolute dissociation efficiency of H₂ in a steady-state H₂–N₂ gas-mixture discharge has been measured by Nagpal *et al.*,²⁴ and their analysis of the energy balance showed that the H₂ was dissociated via a multi-quantum ($\delta v \geq 18$) vibrational energy-transfer mechanism with vibrationally excited ground-state N₂ ($X^1\Sigma_g^+, v$). However, a comparison of the measured H-atom density at 1.0 ns for the 10% H₂ in H₂–N₂ gas mixture with calculations of Gorse and Capitelli²⁵ shows that the calculated N₂ ($v \geq 18$) density buildup by V-V up-pumping is not sufficiently fast. The calculations were for a pure N₂ discharge, with conditions similar to those of the present experiment ($E/n = 60$ Td, $p = 5$ Torr). The calculated N₂, $v = 18$, population is three orders of magnitude lower than the H-atom density, even though the build-up of N₂ vibrational population would be expected to be slightly faster in the calculation, with a higher

E/n value and pressure, than in the experiment. Thus, it appears that vibrationally excited N_2 alone is not responsible for the fractional enhancement in the H_2 dissociation.

Another possible source of energy for heavy-particle energy-transfer dissociation of H_2 is vibrational excitation in H_2 . Although a detailed, self-consistent calculation of the discharge was beyond the scope of the present study, the trend in the vibrational up-pumping in H_2 can be examined by solving a set of vibrational master equations with published V-V and V-T rates.^{26,27} The $H_2(v)$ number densities were estimated by solving the heavy-particle kinetic equations for H_2-H_2 , N_2 , and H-atom V-V and V-T energy-transfer collisions. The calculation was for 10% H_2 in H_2-N_2 , was limited to $v = 0 - 6$ in H_2 and $v = 0$ in N_2 , and was further simplified by fixing the vibrational populations in H_2 , $v = 0 - 2$, and N_2 , $v = 0$, at their initial values. The initial vibrational distributions in H_2 and N_2 were assumed to be Boltzmann, with a vibrational temperature of either 3000 or 3500 K. The temporal evolutions of the H_2 vibrational populations for the two initial vibrational temperatures are shown in Fig. 35. The experimental H-atom densities for 10% H_2 in H_2-N_2 as a function of pulse duration are shown in Fig. 36 (closed circles

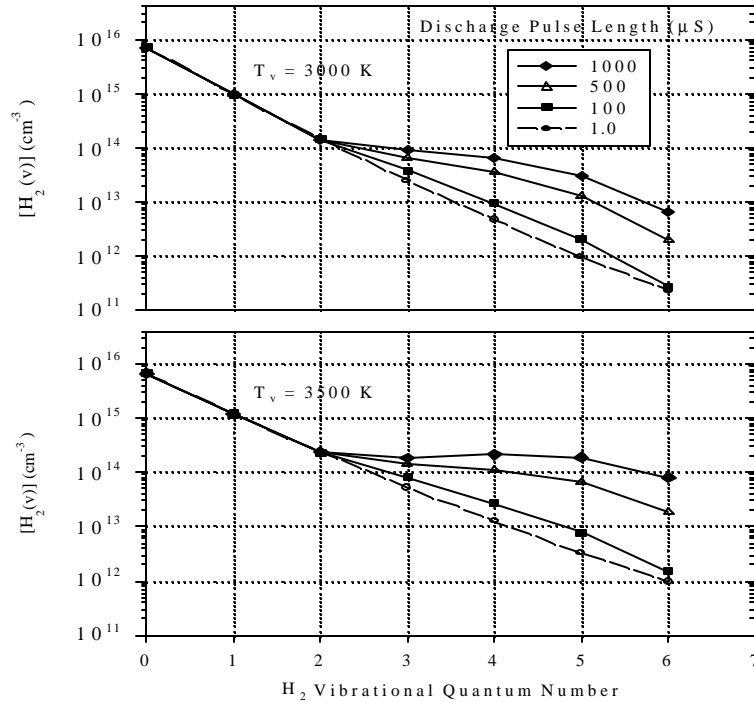


Figure 35. Temporal Evolution of H_2 Vibrational Populations for 10% H_2 in a H_2-N_2 Discharge for Two Initial Vibrational Temperatures.

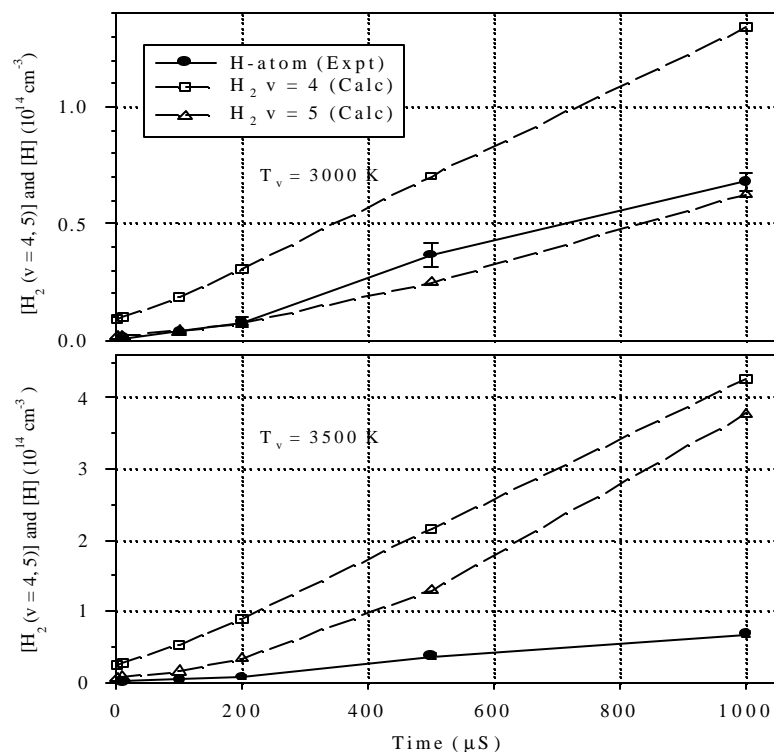


Figure 36. Comparison of the Calculated Temporal Evolution of H_2 , $v = 4$ and 5 , Vibrational Populations for Two Initial Vibrational Temperatures with Experimental H-Atom Densities.

joined by solid lines) along with the estimated H_2 , $v = 4$ and 5 , vibrational populations (open squares and triangles, respectively, joined by dashed lines) for both vibrational temperatures. The calculated H_2 vibrational densities have been multiplied by two for comparison with the H-atom densities. The population in $v = 4$ and 5 is just sufficient to account for the experimental H-atom densities at the lower vibrational temperature, while the populations in both $v = 4$ and 5 are well above the H-atom densities.

Reaction cross sections for H_2 dissociation were calculated from the measured rate of H-atom production at 1.0 ns and the calculated vibrational population densities in H_2 and N_2 . The H_2 vibrational populations were from the present calculation, and the N_2 vibrational populations were taken from Ref. 25. The cross sections were calculated for H_2 , $v = 4$, with N_2 , $v = 10$, and H_2 , $v = 5$, with N_2 , $v = 8$, and a gas translational temperature of 400 K . A cross section for a hard-sphere collision of H_2 and N_2 with molecular diameters of 2.4 \AA and 3.2 \AA , respectively, was also calculated. The results are given in Table 3. Comparison of the determined cross

Table 3

Cross Sections for H₂ Dissociation Determined with Calculated H₂ Vibrational Population Densities Compared to Those Determined with a Hard-Sphere Calculation.

Initial T _v (K)	Cross Section (10 ⁻¹⁶ cm ²)	
	(4,10) ^a	(5,8) ^a
3000	13	3
3500	4	0.5
Hard-sphere ^b	6	

^a (v, v') corresponds to H₂ and N₂ vibrational quantum numbers [H₂(v), N₂(v')], respectively.

^b Hard-sphere cross section calculated with H₂ and N₂ molecular diameters of 2.4 Å and 3.2 Å, respectively.

sections and the hard-sphere cross section shows them to be comparable in size. Only the cross section for H₂, v = 5, and N₂, v = 8, and an initial vibrational temperature of 3000 K is less than the hard-sphere cross section. Thus, a H₂ vibrational distribution that is intermediate between the calculated distributions could account for the experimentally determined H-atom densities. These results suggest that vibrationally excited H₂, v ≥ 4, and N₂, v ≥ 8, may be responsible for the H-atom production through heavy-particle energy-transfer processes in a short-duration pulsed discharge where heavy-particle energy-transfer processes have not reached steady-state equilibrium conditions.

REFERENCES

1. A. I. Klimov, A. N. Koblov, G. I. Mishin, et al, Pis'ma Zh. Tekh. Fiz. **8**, 439 (1982) [Sov. Tech. Phys. Lett. **8**, 192 (1982)].
2. A. I. Klimov, A. N. Koblov, G. I. Mishin et al., ibid, p. 551 [Sov. Tech. Phys. Lett. **8**, 240 (1982)].
3. I. V. Basargin and G. I. Mishin, ibid, **11**, 209 (1985) [Sov. Tech. Phys. Lett. **11**, 85 (1985)].
4. I. V. Basargin and G. I. Mishin, ibid. p. 1297 [Sov. Tech. Phys. Lett. **11**, 535 (1985)].
5. L. P. Grachev, I. I. Esakov, G. I. Mishin et al., Zh. Tekh. Fiz **55**, 972 (1985) [Sov. Phys. Tech. Phys. **30**, 586 (1985)].
6. N. V. Evtyukhin, A. D. Margolin, and V. M. Shmel'v, Khim. Fiz. **3**, 1322 (1984) [Sov. J. Chem. Phys. (1984)].
7. S. A. Bystrov, I. S. Zaslonko, Yu. K. Mukoseev, and f. V. Shugaev, Dokl. Akad. Nauk. SSSR **310**, 70 (1990) [Sov. Phys. Dokl. **35**, 39 (1990)].
8. P. A. Voinvich, A. P. Ershov, S. E. Ponomareva, and V. M. Shibkov, Teplofiz Vys. Temp. **29**, 582 (1991) [High Temp. (USSR) **29** (1991)].
9. P. A. Voinovich, A. P. Ershov, S. E. Ponomareva, and V. M. Shibkov, High Temp. **29**, 468 (1990).
10. Yu. P. Raizer, *Gas Discharge Physics* (Springer, New York, 1997), p. 67; K. Wojacek, Beitr. Plasmaphys. **24**, 209 (1984).
11. A. von Engel, *Ionized Gases* (AIP Press, New York, 1994) (reprint of 1964 Oxford University Press edition), Chap. 8.
12. J. G. Andrews and J. E. Allen, Proc. Roy. Soc. Lond. A **320**, 459 (1971).
13. J. S. Levine and F. W. Crawford, J. Plasma Physics **24**, 359 (1980).
14. P. A. Miller, J. T. Verdeyen, and B. E. Cherrington, Phys. Rev. A **4**, 692 (1971).
15. M. W. Millard, P. P. Yaney, B. N. Ganguly, and C. A. DeJoseph, Plasma Source Sci. Technol. **7**, 389 (1998).
16. W. L. Weise, M. W. Smith, and B. M. Glennon, *Atomic Transition Probabilities, Vol. 1*, National Bureau of Standards Publication No. NSRDS-NBS4 (U. S. Government Printing Office, Washington, D. C., 1966).
17. P. A. Miller, J. T. Verdeyen, and B. E. Cherrington, Phys. Rev. A **4**, 692 (1971).
18. E. A. D. Hartog, T. R. O'Brian, and J. E. Lawler, Phys. Rev. Lett. **62**, 1500 (1989).
19. A. V. Phelps, Phys. Rev. **99**, 1307 (1955).
20. B. E. Cherrington, IEEE Trans. Electron Devices **ED-26**, 148 (1979).
21. S. C. Brown, *Basic Data of Plasma Physics, 1966* (M.I.T. Press, Cambridge, MA, 1967).
22. B. N. Ganguly and P. Bletzinger, J. Appl. Phys. **82**, 4772 (1997).

23. A. Garscadden and R. Nagpal, *Plasma Sources Sci. Technol.* **4**, 268 (1995).
24. R. Nagpal, B. N. Ganguly, P. Bletzinger, and A. Garscadden, *Chem. Phys. Lett.* **257**, 386 (1996).
25. C. Gorse and M. Capitelli, in *Molecular Physics and Hypersonic Flows* (M. Capitelli, Ed.) (Kluwer Academic Publishers, Netherlands, 1996), pp. 437-449.
26. J. Loureiro and C. M. Ferreira, *J. Phys. D: Appl. Phys.* **22**, 1680 (1989).
27. B. Gordiets, C. M. Ferreira, M. J. Pinheiro, and A. Ricard, *Plasma Sources Sci. Technol.* **7**, 363 (1998).

PRESENTATIONS

P. Bletzinger, J. T. Verdeyen, and B. N. Ganguly, "Spatially and Temporally Resolved Measurements of Electron Density Variations Caused by Shockwaves in Plasmas," Poster presented at the 51st Annual Gaseous Electronics Conference, Maui, HI, 19-22 October 1998.

B. N. Ganguly, P. Bletzinger, and A. Garscadden, "Plasma-Shock Interaction in a Low Pressure Positive Column," Presented at the 26th IEEE International Conference on Plasma Science, Monterey, CA, 20-24 June 1999.

J. M. Williamson and B. N. Ganguly, "Hydrogen Dissociation in a H_2 - N_2 Pulsed DC Glow Discharge," Presented at the 52nd Gaseous Electronics Conference, Norfolk, VA, 5-8 October 1999.

A. Garscadden, P. Bletzinger, and B. N. Ganguly, "Acoustic Shock Interaction in a Positive Column Plasma," AIAA Paper No. 99-4973 presented at the AIAA Hypersonics Conference, Norfolk, VA, 1-5 November 1999.

M. Brown, J. Scofield, and B. Ganguly, "Emission and Electrical Measurements to Assess Actinometry in $SF_6/Ar/O_2$ SiC Etching Discharges," Presented at the 53rd Gaseous Electronics Conference, Houston, TX, 24-27 October 2000.

J. M. Williamson and B. N. Ganguly, "He Metastable Density in a Double Layer Formed by a Diameter Discontinuity in a Positive Column," Presented at the 53rd Gaseous Electronics Conference, Houston, TX, 24-27 October 2000.

J. Williamson, B. Ganguly, and C. DeJoseph, Jr., "Gas Temperature Measurements in an Atmospheric Plasma Torch," Presented at the 26th Dayton-Cincinnati Aerospace Science Symposium, Dayton, OH, 30 March 2001.

B. Ganguly, P. Bletzinger, and A. Garscadden, "Shock Wave Propagation in a Non-uniform Medium," Presented at the 26th Dayton-Cincinnati Aerospace Science Symposium, Dayton, OH, 30 March 2001.

P. Bletzinger, B. N. Ganguly, and A. Garscadden, "Mutual Interactions between Low Mach Number Shock Waves and Nonequilibrium Plasma," Presented at the 4th Weakly Ionized Gases (WIG) Workshop, AIAA, Anaheim, CA, 14-15 June 2001.

P. Bletzinger, B. N. Ganguly, and A. Garscadden, "Low Mach Number Shock Wave Induced Modulation of Plasma Conductivity," Presented at the 28th IEEE International Conference on Plasma Science, Las Vegas, NV, 17-22 June 2001.

PUBLICATIONS

P. Bletzinger and B. N. Ganguly, “Local Acoustic Shock Velocity and Shock Structure Recovery Measurements in Glow Discharges,” *Phys. Letts. A* **258**, 342 (1999).

J. M. Williamson and B. N. Ganguly, “Hydrogen Dissociation in a $\text{H}_2 - \text{N}_2$ Pulsed DC Glow Discharge,” *Phys. Rev. E* **61**, 5734 (2000).

P. Bletzinger, B. N. Ganguly, and A. Garscadden, “Electric Field and Plasma Emission Responses in a Low Pressure Positive Column Discharge Exposed to a Low Mach Number Shock Wave,” *Phys. Plasmas* **7**, 4341 (2000).

J. M. Williamson and B. N. Ganguly, “He Metastable Density in a Double Layer Formed by a Diameter Discontinuity in a Positive Column,” *Phys. Rev. E* **64** (2001).